A remarkable Late Saalian (MIS 6) loess (dust) accumulation in the Lower Danube at Harletz (Bulgaria)

Pierre Antoine, France Lagroix, Diana Jordanova, Neli Jordanova, Johanna Lomax, Markus Fuchs, Maxime Debret, Denis-Didier Rousseau, Christine Hatté, Caroline Gauthier, et al.

A remarkable Late Saalian (MIS 6) loess (dust) accumulation in the Lower Danube at Harletz (Bulgaria).

Pierre ANTOINE [a *], France LAGROIX [b], Diana JORDANOVA [c], Neli JORDANOVA [c], Johanna LOMAX [d], Markus FUCHS [d], Maxime DEBRET [e], Denis-Didier ROUSSEAU [f, g], M., Christine HATTÉ [h], Caroline GAUTHIER [h], Olivier MOINE [a], Samuel N. TAYLOR [b], Jessica L. TILL [b, i], SYLVIE COUTARD [j, a].

[a] Laboratoire de Géographie Physique: Environnements quaternaires et actuels, CNRS-Univ. Paris 1-UPEC, 92195 Meudon, France. E-mail: pierre.antoine@lgp.cnrs.fr (* corresponding author).

[b] Institut de Physique du Globe de Paris, Sorbonne Paris Cité, Univ Paris Diderot, UMR 7154 CNRS, 75005 Paris, France.

[c] National Institute of Geophysics, Geodesy and Geography, Bulgarian Academy of Sciences, Acad. G. Bonchev Str., block 3, 1113 Sofia, Bulgaria.

[d] Department of Geography, Justus-Liebig-University Giessen, 35390 Giessen, Germany.

[e] UFR Sciences et Techniques, Université de Rouen 76821 Mont-Saint-Aignan, France.

[f] Laboratoire de Météorologie Dynamique, UMR CNRS-ENS 8539, Institute Pierre Simon Laplace, IPSL, Paris Sciences & Lettres (PSL) Research University, 75231 Paris, France

[g] Lamont-Doherty earth Observatory of Columbia University, Palisades, NY 10964 USA

[h] Laboratoire des Sciences du Climat et de l'Environnement, CEA-CNRS-UVSQ, Université Paris-Saclay, 91198 Gif-sur-Yvette, France.

[i] Institute of Earth Sciences, University of Iceland, 101 Reykjavik, Iceland.

[j] INRAP Hauts-de-France, 32 Avenue de l'Etoile du Sud 80440 Glisy, France.

Abstract

While numerous high-resolution studies concerning Last Glacial aeolian sequences are available for Europe, the approach of the penultimate glacial in this geographical area is still poorly developed. In order to bridge this gap, this study focuses on the Bulgarian sequence of Harletz, along the Danube River, where extremely high sedimentation rates allow the depiction of high-resolution signals during MIS 6. At Harletz in NW Bulgaria on the western bank of the Ogosta River (tributary of the Danube) a 20 m thick loess-palaeosols section was cleaned and sampled for a multi-disciplinary study and detailed pedostratigraphic approach. High-resolution continuous bulk sampling (5 cm) was carried out to characterise sedimentary grain-size, magnetic properties (including magnetic susceptibility and its frequency dependence), colour reflectance (1 cm), and organic carbon. Geochronological control is based on 16 samples collected for OSL and MET-pIRIR dating. Using a cyclo-stratigraphic approach of the sequence combined with dating constraints provided by both MET-pIRIR dates and the age of a tephra layer occurring at a depth of 12m within the main loess Unit, we can demonstrate that the Harletz section exhibits a 10m thick Late Saalian (Marine Isotope Stage 6, MIS 6) loess accumulation unique in Europe. The lower part of the main loess Unit is 4 m thick and overlies a basal brown soil complex allocated to MIS 7, which includes an exceptionally thick (4 m) and detailed succession of loess and four incipient soil horizons never described in European loess until now. The closest and best-dated high-resolution palaeoenvironmental archive suitable for comparison comes from Lake Ohrid located about 400 km to the SW of Harletz. The Ohrid palynological record shows a progressive step-by-step evolution in climate and in environmental change during the transition between MIS 7 and MIS 6 from which a parallel with the Harletz pedosedimentary succession can be proposed. During the younger part of MIS 6 (160-129ka), steppe vegetation with abundant herbs (*Artemisia*) is dominant in the Lake Ohrid record, in good accordance with a global enhancement of aeolian dynamics, especially well recorded in sections located close to the Danube River from Serbia to Bulgaria and Romania (L2 loess). According to interpretations stemming from this study, the silts and fine sands building the Harletz loess section would have been transported from the Danube

braided river system located (at that time) at about 4.5 km to the NW. Based on our data, the main loess Units are characterised by a very low to a total absence of coarse sand particles. By contrast, during the Eemian interglacial (MIS 5e), and to a lesser extent throughout MIS 5 and during MIS 3 interstadials, the long distance transport of silt and fine sand particles is stopped and a weak aeolian sedimentation is likely driven by north-easterly winds transporting coarse sand grains from the proximal Ogosta River sandy banks. Finally, the weak development of Last Glacial loess (4m max.) likely results from a rapid infilling of the sedimentary trap during the Saalian, then followed by a strong anthropogenic erosion of the topsoil and of the upper part of the loess profile since the Early Holocene (Neolithic).

Key words

Pleistocene; Europe; Danube; Saalian; high-resolution; luminescence dating; grain-size; magnetic susceptibility.

1. Introduction

The impact of rapid climatic events such as the Dansgaard-Oeschger (D-O) cycles on records of European environments during the Last glacial has been the focus of many research studies over the last 20 years (Sánchez Goñi et al., 1999, 2002, 2008; Müller et al., 2003; Desprat et al., 2007; Seelos et al., 2009; Boch et al., 2011; Moreno et al., 2014; Heiri et al., 2014; Luetcher et al., 2015). Bringing valuable contributions to this collective effort are investigations of European loess sequences based on multi-proxy analyses, continuous high-resolution sampling and luminescence and ^{14}C dating (Antoine et al., 2001, 2009a; Haesaerts et al., 2003; Rousseau et al., 2007, 2011; Gocke et al., 2014; Ujvari et al., 2014, Moine et al., 2017). Studies of loess sequences have provided evidence of the extreme sensitivity of European environments to millennial climatic cycles (D-O Cycles) during the Last Glacial (Hatté et al, 1998; Antoine et al., 2001, 2009a,b, 2013, 2016; Moine et al., 2002, 2008; Rousseau et al., 2002, 2007, 2011, 2017a,b). Continued loess investigations searching to resolve the

impact of D-O climate cycles systematically from north-western to central Europe now logically move towards the Lower Danube loess area (Fig. 1A), well known for its very thick loess sections as in Serbia (Titel Plateau: Markovic et al., 2009, 2015; Varga et al., 2012; Surduk: Fuchs et al., 2007; Antoine et al., 2009b) or in the Czech Republic (Dolni-Vestonice: Antoine et al., 2013, Rousseau et al., 2013; Zeměchy: Hošek et al., 2015, Dunaszekcso: Újvári et al., 2018).

The above-mentioned studies have predominantly focused on Last Glacial dust accumulation. Throughout Europe, investigations of Penultimate glacial loess sequences are sparse (Kukla, 1977; Markovic et al., 2015; Hérisson et al., 2016) despite observations of rapid (millennial) climatic variations during marine isotope stage (MIS) 6 (ca. 170 and 140 ka) in marine sediment records (Martrat et al., 2004, 2007; Margari et al., 2010; Baker et al., 2011; Mokeddem and MacManus, 2016), in lacustrine continental records (Sirocko, 2016; Sadori et al., 2016; Francke et al., 2016), and even in Chinese loess sequences (Yang and Ding, 2014). To bridge this gap, Bulgarian loess sequences are potentially ideal candidates. Located in the Lower Danube area, approximately 300 km downstream of the Titel Plateau in Serbia (Fig. 1B), important loess accumulations up to 40-60 m in thickness spanning the last 780 ka can be found (Jordanova et al., 2007, Jipa, 2014). Moreover, especially thick (> 6 m) MIS 6 (or L2) loess Unit is preserved in this area. Despite the great potential of Bulgarian loess, there are few documented studies (Jordanova and Petersen 1999; Jordanova et al., 2008) and the sequences' chronologies are weakly constrained (Avramov et al., 2006). In 2012, a group of multi-disciplinary researchers in collaboration with the Bulgarian Academy of Science aimed to remedy the situation. Thick loess sequences spanning many hundreds of thousands of years covering the eastern parts of Bulgaria and Romania (Radan, 2012) were investigated. In northwestern Bulgaria, in the vicinity of the village of Harletz, loess thicknesses covering the T2 terrace are lesser, on the order of 20 m, but they also span a shorter time period based on magnetic susceptibility stratigraphic correlations (Avramov et al., 2006), thus resulting in higher resolution records.

101 The sequence of Harletz (43°41'52.78" N / 23°49'42.27" E / altitude ca. 40m a.s.l.) is located on the
102 left bank of the Ogosta River, about 7 km to the southeast of its confluence with the Danube (Fig. 1B,
103 2). The studied section is a natural sub-vertical (ca. 70°) outcrop resulting from the erosion of the
104 loess cover in the concavity of a meander of the Ogosta River, currently inactive. Owing to the very
105 good preservation of the meander bars in the present-day alluvial plain, this erosion likely occurred
106 during the Holocene (Fig. 2). The geology of the area has been investigated in detail (Evstatiev et al.,
107 2000; Evlogiev, 2015) motivated by the Kozloduy Nuclear Power Plant, located 6 km to the east-
108 northeast on the right bank of the Danube (Fig. 2). The Harletz loess sequence, thus, overlies an
109 alluvial terrace body (sand and gravels) corresponding to the T2 level of Evlogiev (2015) (Fig. 3). The
110 basal contact between these fluvial sediments and the bedrock (Pliocene silty clay) is located at
111 about 25 m above sea level, at a similar altitude than the top of the current flood plain of the Danube,
112 in a slightly stepped-terrace configuration whose morphology is largely hidden by a loess cover as
113 thick as 40 m in the upper part of the slope (Fig. 3, Evstatiev et al., 2000). In the absence of accurate
114 topographic data for the Ogosta River valley, we rely on *Google Earth* altitudes based on the 2015
115 copyrighted CNES image provided by the SPOT 5 satellite which has a in plane accuracy of 10 m and a
116 vertical accuracy of 5 m, comparable with conventional 1:50 000 scale mapping. The Ogosta River
117 (surface: ca. 30 m a.s.l.) is currently weakly incised (ca. 2-3 m lower) with respect to the base of the
118 Harletz loess-palaeosol sequence.
119 The area is presently characterized by a continental climate with mean annual temperature of 11°C,
120 mean January temperature of - 2°C, and mean July temperature of 23°C (Fotakiewa and Minkov,
121 1966). Mean annual precipitation ranges between 500-600 mm per year with a maximum in the
122 summer months. Present topsoil is a typical Chernozem but since the Early Neolithic it has repeatedly
123 been partially or totally eroded by human activity (Giosan et al., 2012).
124 The aim of this paper is to:

1) Present a detailed overview of the pedo-stratigraphy and sedimentology of the Harletz record including comparisons with magnetic susceptibility, TOC, $CaCO_3$ and colour reflectance data and luminescence dating and discuss both palaeoclimate and palaeoenvironmental implications.

2) Correlate the Harletz loess sequence with other European sequences as well as with other continental and marine palaeoclimate and palaeoenvironmental records that have geochronologically well-constrained palaeoclimate signals.

2. Material and methods

2.1. Field description and sampling

The vertical section was exposed by intensively removing the thick accumulation of reworked loess debris, which accumulated naturally on the steeply (ca. 70°) sloping concave meander wall carved by the Ogosta River. The section excavation resulted in 8 vertical panels of 2 to 3 m in height forming a series of steps carefully connected and metered using a hand-level (Fig. 4). The Harletz sequence totals 20 m in vertical depth and was continuously and accurately logged (scale of field drawing: 1/10). Colour is a fundamental parameter for the description of loess-palaeosol sequences, controlled by variations of the major mineral and organic components of soils and sediments: quartz, carbonates, iron and Fe-Mn oxides and oxyhydroxides and organic matter. Their relative variations are directly driven by climate and environmental conditions. The detailed and coloured log drawn from the Harletz section, shown in Figure 5, follows an original approach developed (e.g. Haesaerts et al., 2003, 2016; Antoine et al., 2009a,b, 2013) to produce more realistic and useful logs of investigated sections than the traditionally published (over) simplified black (soil and palaeosol) and white (loess) sequence logs.

Bulk sampling for sedimentological, magnetic and geochemical analyses followed the continuous column sampling methodology (Antoine et al., 2009a) with a 5 cm depth-resolution. An extruding column with an approximate cross-section of 5 x 6 cm was sliced every 5 cm to produce homogenized bulk samples of about 300 grams. This step was conducted with extreme caution

avoiding and (or) systematically removing traces of biotubules that may pollute the analytical signal with their clayed-humic infillings originating from surface material. A total of 400 bulk samples were collected. In addition, a set of 10 undisturbed blocks where extracted from various soil horizons and sediments for thin section preparation and micromorphological observations. These along with other field observations are summarised in Table 1.

2.2. Sedimentological analyses

2.2.1. Grain size

Grain size analyses were performed with a Coulter LS-230 operating at the CNRS Meudon laboratory and followed the protocol developed for the study of European loess sequences (Antoine et al., 2009a). Ten grams of bulk sample was homogenized, dispersed in a solution of sodium hexameta-phosphate, and placed in a rotary shaker for two hours. The sediment is sieved at 160 µm to remove coarse sand grains, calcareous concretions and other debris from calcified roots or mollusc shells, which may disturb the results of laser analysis. The mass of the larger than 160 µm fraction is reported as a percentage of the initial sample mass (10 g). Coulter LS-230 analyses are conducted on the less than 160 µm fraction and calibrated on a series of 17 test samples representative of the various facies following the standard Robinson sieving and pipette method (Soil Analysis Laboratory of INRA-Arras, Table 2). Such a calibration is particularly important with regards to clay content and determining the upper limit of clay grain size of laser data. For the Harletz sequence, the calibration results in clay sizes extending to 6 µm for the Coulter LS-230 data, in accordance with previous results on similar type of sediment (Konnert and Vandenberghe, 1997; Antoine et al., 2013), whereas classically the upper clay grain size is set at 2 µm. Finally, two grain size ratios are calculated: Grain Size Index (GSI) of Antoine (2009a) defined as the ratio between coarse silts (20-63µm) and the sum of fine silts (6-20µm) and clays (≤ 6µm) and Coarse Silt Index (CSI) of Schirmer (2016) defined as the ratio between coarse silts (20-63 µm) and fine silts (6-20µm).

177 ***2.2.2.*** **Organic and carbonate content**

178 The sediment samples (400) were dried out at low temperature as soon as possible to ensure safe
179 storage, as recommended by Gauthier and Hatté (2008). After being sieved at 200 µm to remove
180 coarse sand grains, $CaCO_3$ concretions (calcified root tracks) and mollusc shells, and being
181 homogenized, the sediment then underwent a soft leaching process to remove carbonate using pre-
182 combusted glass beakers, HCl 0.6N at room temperature, ultra-pure water and drying at 50°C. The
183 samples were then crushed in a pre-combusted glass mortar for homogenization prior to carbon and
184 carbonate content evaluation. The handling and chemical procedures are common precautions
185 employed with low-carbon-content sediments.

186 Two different carbon measurements were performed for every sediment sample: total carbon for
187 the bulk sediments and organic carbon for the leached sediments. Approximately 15 to 20 mg of
188 sediment was weighed in tin cups for measurement (with a precision of 1 µg). The sample was
189 combusted in a ThermoFinigan Instrument Flash EA 1112 Elemental Analyser, and the carbon
190 content determined using the Eager software.

191 A standard was inserted as unknown every 10 samples. The inorganic carbon content in the bulk
192 sediment was calculated by assuming that mineral carbon exists only as $CaCO_3$. The results are
193 reported in %weight of carbonate/bulk sediment and in %weight of organic carbon/bulk sediment
194 and shown in Figure 5.

195

196 **2.3. Spectrocolorimetry**

197 Spectrocolorimetry enables to quantify colour changes, not perceptible with the naked eye, through
198 the acquisition of very high-resolution colour reflectance spectra (e.g.: Unit 1b, Fig. 5). The low
199 purchase and maintenance costs and especially the portability of some spectrocolorimeters enables
200 analyses to be acquired directly in the field and has been shown to be a powerful tool in combination
201 with sedimentological observations (see Debret et al., 2011 for a review). At present, the CIELAB
202 system more commonly referred to as L*a*b* system is the most widely used approach in

sedimentology to report colour reflectance spectra data. The colour space it defines can be visualised in a spherical coordinate system where each of the three axes represent one of the three variables: lightness (L*) ranging from 0% to 100%, green – red chromaticity (a*) where green is negative and red is positive, and blue – yellow chromaticity (b*) where blue is negative and yellow is positive. All the data (Fig. 5) were acquired with a Minolta CM 2600d over the extended visible wavelength domain from 360 to 740 nm and operating with a 6504 K light source. The sensitivity of the device allows wavelength spectrum resolution of 10 nm. The a* parameter tracks variations related to the redness of the sediment (Fig. 5) and was postulated by Ji et al. (2004) to proportionally vary with hematite of pedogenic origin associated with clays. In the present study, we combine a* with clay percentage, magnetic susceptibility values and thin sections observations, where a* is considered as a proxy of the intensity of the weathering and of soil formation processes.

Measurements in the field were conducted at a 1 cm depth resolution. For the purpose of comparing spectrocolorimetry data with other proxy data acquired along HZ12 at a 5 cm depth resolution bulk samples, the variables a*, b* and L, across a bulk sample interval (n = 5), were averaged and their standard deviation calculated.

2.4. Magnetic susceptibility

The in-field volume-specific magnetic susceptibility (κ_{FIELD}) was measured with a handheld KT-6 Kappameter from SatisGeo (Brno, Czech Republic) along the entire section at a 10 cm depth interval. Five measurements were made evenly spaced across approximately one meter in width at each stratigraphic level. Mean values and standard deviations were calculated. Laboratory measurements of the mass-specific magnetic susceptibility (χ_{BULK}) was analysed on the bulk samples at a 5 cm depth interval with a Bartington MS2B dual frequency bridge operating with a field amplitude of 200 A/m and at frequencies of 465 Hz and 4650 Hz. Bulk material was homogenized and compacted in 8 cm^3 plastic boxes. The absolute frequency dependence of magnetic susceptibility ($\Delta\chi_{FD}$) is the difference between the low-frequency and the high-frequency mass specific magnetic susceptibility. $\Delta\chi_{FD}$ is a

measure of the concentration of magnetic particles of grain size near the superparamagnetic (SP) to stable single domain (SSD) threshold at room temperature (30 nm). Within a loess and palaeosol sequence magnetic particles of this size are considered to be of pedogenic origin (Maher and Taylor, 1988; Zhou et al. 1990) and $\Delta\chi_{FD}$ is expected to increase with increasing degree of pedogenesis if mean annual precipitation does not exceed 1200 to 1500 mm/yr (Thompson and Maher, 1995; Balsam et al., 2011) and in the absence of other diagenetic alteration process (e.g. Taylor et al., 2014).

2.5. Luminescence dating

16 samples were taken at night for luminescence dating, by scraping unexposed sediment into black plastic bags (e.g. Fuchs et al., 2013). It was attempted to avoid areas affected by bioturbation, although this was nearly impossible in the upper part of the section. Consequently, some mixing of layers of different sedimentation ages is to be expected in the upper 1.5m of the section. Additional samples were taken from the surrounding sediment for dose rate determination, comprising representative material within a 30 cm radius around the luminescence sample.

Samples for luminescence dating were prepared by separating the fine grain quartz fraction (4-11 µm) and the coarse grain potassium feldspar (K-FS) fraction (63-200 µm). Sample preparation for both separated fractions is described in Lomax et al. (2014a). All measurements were performed on a Lexsyg Research Luminescence reader (Lomax et al., 2014b).

The fine grain quartz samples were analysed using a standard SAR protocol (Murray and Wintle, 2000; 2003), with preheat and cutheat temperatures set at 220 and 200 °C respectively. Coarse grain feldspar samples were measured using the MET-post-IR-IRSL (MET-pIRIR) protocol (Li and Li, 2011).

Radionuclide concentrations of U and Th were determined using alpha counting and K concentrations using ICP-OES. These analyses were carried out at the University of Bayreuth (Department of Geography). For further details, see Lomax et al. (2018).

2.6. Radiocarbon dating protocol of gastropod shells.

255 Land snail shells (*Helicopsis striata)* were slightly crushed in an agate mortar. All samples were
256 leached with 0.01M HNO_3 at room temperature for at least 30 min and rinsed with Milli-Q water to
257 remove superficial contamination and oxidize any remaining organic matter. Extra water is removed
258 using a Pasteur pipette. Samples were then introduced into the bottom of a two-fingers reactor
259 (Tisnérat-Laborde et al. 2001) and 1 cm^3 of pure H_3PO_4 (100%; previously distilled for 3 days at 105 °C
260 and stored under argon) is added into the lateral reservoir. The reactor with the wet sample and
261 H_3PO_4 is rapidly connected to the semi-automated vacuum line. The sample is then dried on the line,
262 and the reactor is manually rotated to pour H_3PO_4 onto the samples. Subsequent steps are: CO_2
263 evolving, water elimination, and evaluation of C quantity. CO_2 reduction and ^{14}C activity
264 measurements are performed in Saclay (Cottereau et al. 2007). Results are expressed according to
265 Stuiver and Polach (1977).
266

267 ## 3. Results

268 ### 3.1. Stratigraphy

269 The detailed pedostratigraphic study of the profile describes a sequence composed of 14 main Units
270 over the 20 m of its thickness (Fig. 5). Some of the main micromorphological features from the
271 various soil horizons and loess layers are shown in Figure 6. From the top to the base, the
272 pedostratigraphic sequence of Harletz is composed of the following succession described below in
273 Table 1.

Units	Description (field and thin sections)	Pedosedimentary interpretation
0	Brown greyish to blackish sandy silts with granular structure and numerous fine root tracks. Sharp basal contact. In a lateral profile, the base of this horizon is strongly bioturbated by numerous tacks of burrowing animals (about 5 cm in diameter).	Ploughing horizon of the surface Chernozem soil (topsoil). In a lateral profile, this horizon is thicker (0,4m), darker, and corresponds to an in situ Ah horizon of Chernozem.

1a	Light brownish calcareous sandy silt with abundant root tracks and biogalleries with black clayey coatings and large burrows up to 5 cm in diameter.	Upper part of loess Unit 1b with abundant bioturbations originating from the topsoil. Evidences of weak pedogenic processes (higher χ_{BULK} / TOC and clay values) prior to topsoil formation.
1b	Light brown calcareous sandy silt with numerous root tracks and biogalleries with black clayey coatings and burrows up to 5 cm in diameter. Scattered little $CaCO_3$ concretions ("loess dolls" ≤ 1 cm) between 0.8 and 1.1 m depth.	Sandy loess strongly affected by bioturbation resulting from the biological activity of the surface soil (C_{Ca} calcic horizon of the eroded surface soil)
1c	Light brown calcareous sandy silt with numerous root tracks and biogalleries with black clayey coatings.	Weakly weathered sandy loess (mainly evidenced by grain size, spectro-colorimetry and χ_{BULK} parameters), polluted by recent bioturbations infilled by clayey-humic coatings originating from the surface organic horizon
1d	Pale light brown homogeneous calcareous sandy silt with scattered root tracks and biogalleries with dark clayey coating (insects / earth-worms). In depth, this Unit appears less and less affected by bioturbations. Small calcareous concretions (≤ 2 cm) at the base.	Typical calcareous sandy loess polluted by recent bioturbations (insect galleries), partly infilled by clayey-humic coatings originating from the surface organic horizon.
2a	Brown to brown greyish compact clayey sandy silt	B-horizon of steppe soil intensely

	with strong granular structure (2-3 mm), apparent coarse sand grains (1-2 mm). Abundant fine roots porosity (≤ 1 mm) and mollusc shells. Bioturbated upper limit with large galleries (crotovinas) in the upper 10-15 cm. Discontinuous small stone line (≤ 5mm) at the basal boundary with 2b. TOC: 0.4 %.	bioturbated and developed on colluviated coarse sandy silts. This horizon corresponds to an argic to cambic horizon of a luvic Cambisol (or luvic Phaeozems) (FAO-UNESCO, 2014).
2b	Brown to brown greyish compact clayey sandy silt with strong coarse granular structure and aggregates (2-5 mm) and « crunchy facies ». Abundant *in situ* fine porosity (≤ 1 mm) roots and bioturbations (1-2 mm) by insects (and earthworms?). Strong secondary $CaCO_3$ accumulation in the lower 30 cm (matrix and nodules ≤ 1 cm). $CaCO_3$ up to 20-25%. Lower boundary strongly bioturbated with large galleries excavated by burrowing animals into the underlying loess (diam.: 5-10 cm).	B-horizon of intensely bioturbated steppe soil developed on sandy loess. This horizon corresponds to an *in situ* Bv horizon of a Cambisol, the intensity of which appears in thin section stronger than in the overlying Unit 2a.
3a	Light grey brown homogeneous calcareous sandy silt with numerous scattered mollusc shells (6 - 7 m). Some large burrows with loess infilling. Biogalleries with clayey-humic coatings originating from the soil horizon 2b. Upper 0.5 cm very rich in secondary carbonate (matrix) and concretions ($CaCO_3$: 20-24%).	Calcareous sandy (fine sands) loess, with weak (incipient) syn-sedimentary pedo-genesis developed prior to the overlying 2b soil), indicated by sedimentological and magnetic parameters (clay-TOC- χ_{BULK}). Strong secondary $CaCO_3$ accumulation in the upper 0.5 cm (CCa horizon of soil 2b).

3b	Light brown to yellowish homogeneous calcareous sandy silt with rare thin (1-2 mm) and discontinuous sandy laminations between 10.5 and 12 m. Although not visible during field works a tephra layer has been identified in this unit by magnetic parameters at -12m depth, see: *4.1.2.1.2*)	Typical calcareous sandy loess (fine sands) with high accumulation rate.
4	Light brown to light greyish brown massive calcareous sandy silt with strong fine root tracks porosity (≤ 1 mm), pseudomycelium, little Fe-Mn concretions and Fe-Mn coatings on biogalleries.	Incipient (embryonic) humic soil horizon (rooting Hz. with lowering of the loess deposition rate).
5	Light brown massive homogeneous calcareous (fine) sandy silt.	Typical homogeneous sandy calcareous loess
6	Light brown to light greyish brown massive calcareous sandy silt strong fine root tracks porosity (≤ 1 mm), pseudomycelium, little Fe-Mn concretions and Fe-Mn coatings on biogalleries. Bioturbated basal contact with Unit 7.	Incipient (embryonic) humic soil horizon (rooting Hz. with lowering of loess deposition rate). The weathering appears more developed than in the incipient soil of Unit 4.
7	Light brown massive homogeneous calcareous (fine) sandy silt.	Typical homogeneous sandy calcareous loess
8	Light brown to light greyish brown massive calcareous sandy silt with strong fine root tracks porosity (≤ 1 mm), pseudomycelium, little Fe-Mn concretions and Fe-Mn coatings on biogalleries, diffuse lower boundary.	Incipient (embryonic) humic soil horizon (rooting Hz. with lowering of the loess deposition rate). The weathering intensity appears more or less the same than in the incipient soil of Unit 6.

9	Light brown massive homogeneous calcareous (fine) sandy silt with scattered pseudomycelium and numerous Fe-Mn concretions (≤ 1 mm) in the upper 20 cm.	Typical homogeneous sandy calcareous loess with more marked rooting evidences.
10	Homogeneous brown to grey brownish sandy silt with fine granular structure. Abundant fine root tracks (≤ 1 mm), pseudomycelium and little Fe-Mn concretions and Fe-Mn coatings on biogalleries. Strongly bioturbated lower boundary (30cm) with large burrows (5-10cm).	Steppe soil horizon (cambic Hz.?) markedly more developed than Units 4, 6 and 8 showing a strong bioturbation by burrowing animals at the base.
11	Light brown to whitish massive sandy calcareous silt with numerous $CaCO_3$ concretions and deep calcium carbonate impregnation on root tracks ($CaCO_3$: 22-24%). Numerous large biogalleries filled by material originating from the overlying soil horizon.	Homogeneous sandy calcareous loess enriched in $CaCO_3$ in relation to the overlying soil of Unit 10 (calcic horizon C_{Ca}) and deeply bioturbated by burrowing animals.
12	Brown compact clayey coarse sandy silt weakly calcareous ($CaCO_3$: 12-15%), with diffuse granular structure, scattered mollusc in the upper part, including debris of large terrestrial species (*Cepaea* sp.). Strong bioturbation with very abundant biogalleries and casts. A few discontinuous sandy layers. Very progressive transition with the underlying level 13a.	Fluvial sandy clayey (overbank deposits) with a well developed pedogenesis (cambic horizon) and strong bioturbation by insects and earthworms (upbuilding / aggrading soil of alluvial plain).
13a	Brown clayey coarse sandy silt slightly lighter than	Bioturbated fluvial sandy clayey silts

	Unit 12 with scattered (terrestrial) mollusc shells, some from large species (4-6 mm). $CaCO_3$: 12-13%. Well-marked thick coarse to medium sand laminations (> 1 cm), *in situ* bioturbation less developed than in Unit 12.	(overbank deposits) weakly affected by soil processes (Bw horizon of Cambisol)
13b	Brown and very compact clayey coarse sandy silt with a few scattered sandy layers and diffuse granular structure. $CaCO_3$: 12-13%). Strong bioturbation with very abundant biogalleries and casts (stronger than in 13a). Mollusc shells including debris of large terrestrial species (Cepaea sp.). Sharp lower boundary underlined by a coarse sand layer.	Fluvial sandy clayey silts (overbank deposits) affected by pedogenesis (Bv horizon of Cambisol) and strong bioturbation by insects and earthworms (upbuilding soil dynamics less marked than in 12).
14	Brown and very compact clayey coarse sandy. Strong bioturbation with very abundant biogalleries and casts. Prismatic structure with thick reddish clayey coatings. Numerous scattered $CaCO_3$ concretions (2-8 cm) mainly between 19 and 19.5 m (matrix $CaCO_3$: 4-7%). The occurrence of numerous scattered stones at the base of this Unit indicates the proximity of the underlying alluvial gravels.	*In situ* Bt horizon of leached Cambisol (leached Phaeozen) developed on fluvial sandy clayey silts (overbank deposits).

274

275 **Table 1**

276 Stratigraphy of the Harletz loess sequence: description of the Units and pedosedimentary

277 interpretation, from top to bottom

3.2. Sedimentology

Results of the grain size analysis are presented in Figure 5 along side of the stratigraphic log and summarized through data profiles of clay (≤ 6 μm) percentages, CSI, GSI, fine sand (63-160 μm) and coarse sand (> 160 μm) percentages. Overall, we note a very good correlation between the structures recorded by the various sedimentological parameters and the pedostratigraphy, even at the scale of very thin units as the micro-soil of unit 6 (Fig 5). The detailed description of these variations regarding to the pedostratigraphic succession is included hereafter in the first part of the discussion (part 4.1).

3.3. Magnetic susceptibility

Profile data of laboratory analyses of magnetic susceptibility (χ_{BULK} and $\Delta\chi_{FD}$) are plotted in Figure 5 along side the stratigraphic log of the Harletz sequence.

The large-scale variations observed in the κ_{FIELD} data (see Figure 2 in Lomax et al., 2018) are reproduced in the higher resolution laboratory data in which finer-scale structures are revealed. The two welded soils of Unit 2 are well resolved as well as the series of incipient soils of Units 4, 6, and 8. Of these, only Unit 6 is observed in κ_{FIELD}. χ ranges from minimum values of 25 x 10^{-8} m^3/kg across the lower and middle parts of loess Unit 3 to maximum values of 100 x 10^{-8} m^3/kg at the top and base of palaeosol Units 2b and 2a, respectively (Fig. 7). In a previously studied section located a few hundred of meters away on a carved cliff face of a downstream meander of the paleo-Ogosta river (Avramov et al. 2006), χ values across the prominent Unit 2 palaeosols peaked at 50 x 10^{-8} m^3/kg, which is half of HZ12 values. Indeed, Avramov et al. (2006) reported the occurrence of an incipient soil at an equivalent stratigraphic depth to HZ12 Unit 2. Otherwise, the reported data for these two proximal sections describe similar variations and both capture the sharp increase in χ at the base of Unit 3 (ca. 13 m depth in Avramov et al., 2006 section).

Pedogenic neo-formation of iron oxides may be tracked with $\Delta\chi_{FD}$ and $\%\chi_{FD}$ where their magnitudes are generally proportional to the relative concentration of superparamagnetic (SP) particles (Dearing

et al., 1997). It is however noteworthy to remember that the magnitude of χ_{FD} is also dependant on magnetic grain-size distribution where for the same absolute concentration of SP particles but having a grain size distribution of greater width will have a lower χ_{FD} (Eyre, 1997). Along HZ12, the mean $\Delta\chi_{FD}$ is 3.10 ± 2.67 x 10^{-8} m^3/kg with minimum and maximum values of 0.06 x 10^{-8} m^3/kg and 10.0 x 10^{-8} m^3/kg respectively. The mean χ_{FD} is 5.2 ± 2.8 % with minimum and maximum values of 0.2 % and 11.0 % respectively. The sharp peak in χ at the base of Unit 3 is not coupled with elevated values of $\Delta\chi_{FD}$ and χ_{FD} as observed for Units 14 through 10, the upper parts of Unit 3, Units 2a and 2b, the upper two-thirds of Unit 1 and the topsoil.

Plotting $\Delta\chi_{FD}$ against χ displays an overall linear correlation with an R^2 of 0.96 but breaks in the data distribution are evident at χ values of ca. 40 x 10^{-8} m^3/kg and 70 x 10^{-8} m^3/kg delimiting three groups (Fig. 7) which coincides with discrete stratigraphic units. The group with the highest values of χ_{BULK} and $\Delta\chi_{FD}$ is composed of three continuous depth intervals: 18.65 – 15.75 m, 5.75 – 4.25 m, and 0.35 – 0 m. These horizons correspond to the highest degree of pedogenic development within the basal fluvial soil complex (Units 13 and 12), the Harletz Soil Complex (Unit 2a-2b) and upper part of the topsoil. Moderate levels of pedogenic alterations or poor preservation of pedogenic fine-grained magnetic mineral (i.e. Unit 14) are suggested for depths with mid-range values of χ_{BULK} and $\Delta\chi_{FD}$. The moderately altered loess depth intervals are: 15.75 – 14.60 m (Units 11 and 10), 6.65 – 5.75 m (upper part of Unit 3a and lower part of Unit 2b), 4.25 – 4.10 m (top of Unit 2a), 3.15 – 0.35 m (Units 1c, 1b, and 1a). Low $\Delta\chi_{FD}$ values are associated with the least altered or pristine loess intervals with equally low χ_{BULK} and clay percentages (Fig. 8B) and unimodal grain-size curves (Fig. 9A). Unaltered loess deposits are preserved over two continuous depth intervals, 14.50 – 6.65 m and 4.10 – 3.15 m, but excludes the 12.10 – 12.00 m depth interval (see below and Section 4.2.1). The former corresponds to the loess and incipient soils of Units 9 through 4 and the massive loess of Unit 3b and the base 3a of Saalian glacial age; while the later corresponds to Weichselian age loess of Unit 1d. The incipient palaeosols (Unit 8, 6, 4) and underlying loess (Unit 9, 7, 5) have $\Delta\chi_{FD}$ and χ_{FD} that are

undistinguishable from those of unaltered loess. This said small variations in $\chi_{□□□□}$ and clay % do display local highs for Unit 8 and 6 as well as at 12.60 m depth midway through loess Unit 5. A local high associated with the incipient palaeosol of Unit 4 is masked by the sharp peak in $\chi_{□□□□}$ at the base of Unit 3. As stated above, this peak is not associated with any frequency dependence of magnetic susceptibility even though with a $\chi_{□□□□}$ of 46 x 10^{-8} m^3/kg this layer should behave similarly to the Group 2 population. This anomalous layer is likely the result of a thin tephra fall layer or tephra material mixed in with the loess (see Section 4.2.1).

The interpretation of $\Delta\chi_{FD}$ as a proxy for the degree of pedogenesis is compared and cross-checked with clay content and a* (Fig. 8). Like $\Delta\chi_{FD}$, both clay % and a* are expected to increase with increasing degree of pedogenesis; the former as a result of mineral weathering and the latter as a result of increased reddening of the sediment. The relationship between clay % and the relative concentration of superparamagnetic particles ($\Delta\chi_{FD}$), shown in Figure 8B, is linear with an R^2 of 0.85 and a y-intercept of 15.4 %, which coincides with background clay % values across unaltered loess of Unit 3b. The relationships between a* and clay % or $\Delta\chi_{FD}$ are more complex, yet not random, and allow to further discriminate between the various pedogenic units as well as loess units (Figs. 8A, C). For example, the basal fluvial soil complex in Figure 8C plots as three distinct modes where the mode centred on a* values of 6 correspond to Unit 12, the mode centred on a* values of 9 correspond to Unit 13, and the mode centred on a* values of 8 correspond to Unit 14.

3.4. Luminescence dating

Luminescence ages for the quartz fine grain and feldspar coarse grain fractions are shown in Table 3 and in first in Fig. 5. The reader is referred to Lomax et al. (2018) for a more comprehensive reporting of Harletz luminescence ages. They demonstrated that the quartz ages for the upper part of the sequence (Unit 1a-d) and the underlying palaeosol Unit are reliable, and that all older ages are underestimated, since doses in these samples exceed the saturation level of 200-300 Gy estimated by Timar-Gabor and Wintle (2013). In Figures 5, 10, 11 and 12 we reported the four quartz ages from

the upper 4.6m of the section that are considered as reliable (italics) and the nine feldspar ages (bold) from -1.35 to -19.75m (bold). The feldspar ages that appear strongly underestimated owing to both their position below the tephra layer (identified at -12m by magnetic parameters and correlated with the Vico B-ignimbrite, see: *4.1.2.1.2*) and their stratigraphic location regarding to the basal soil complex are in bold italic with a superscript star.

In case of the feldspar extracts, equivalent dose (D_e) determination was hampered due to the lack of a D_e plateau within the MET-pIRIR measurements for most of the samples. A pIR stimulation temperature of 150°C showed a good match with quartz ages in the upper part of the profile. Based on this observation, all feldspar ages which build up the chronology of the lower part of the section, are based on pIR stimulation temperatures of 150°C (Lomax et al., 2018). The two lowermost ages show an age inversion and, compared to overlying ages, appear greatly underestimated. The reason for this is unclear, but may relate to both the underestimation of the water content and overestimation of the dose rate. The water content estimation is especially difficult for the basal soil complex (12 to 14) developed mainly as upbuilding soil horizons in a flood plain environment subject to regular flooding events.

4. Discussion

4.1. Pedostratigraphy and palaeoenvironments

The combination of high-resolution pedostratigraphy, grain size studies, and of additional analytical parameters (χ_{LF}, $\Delta\chi_{FD}$, Colour reflectance, TOC and $CaCO_3$), throughout the whole sequence, shows a very good correlation between all proxies and the stratigraphic boundaries defined in the field (Fig. 5). Some very thin (ca. 10 cm) horizons like the micro-soils of Units 4 or 8 especially well illustrate this characteristic (Fig. 5). In addition, variations in both clay percentage and GSI, combined with parameters as a* values, TOC percentage or magnetic parameter, enable to highlight variations within the sediments which were not visible in the field despite a very detailed observation. A good example is given in the upper part of the profile (Unit 1a to 1d, Fig. 5).

From a global pedo-sedimentary point of view, the Harletz sequence appears to be composed of two main parts corresponding to two contrasted environments, from the base to the top:

1) A basal fluvial soil complex (Ogosta Soil Complex), dominated by low dynamic fluvial sedimentary processes of alluvial plain (overbank deposits), associated with more or less contemporary pedogenic processes (Units 14 to 12).

2) A loess-palaeosol sequence (LPS), dominated by aeolian sedimentation (loess) more or less sandy (Units 11 to 3b and 1d-1a), interrupted by a succession of weakly developed soils (incipient soils) at the base (Units 10, 8, 6, 4). This sequence is divided in two parts by a well-developed 2 m thick soil complex (2a-2b Units, Harletz Soil Complex) and is overlaid by a strongly truncated topsoil (Unit 0).

4.1.1. Basal fluvial soil complex (Ogosta Soil Complex) (Units 14-12)

This part of the record corresponds to a thick (4.7 m) brown sandy-clayey pedosedimentary complex in which χ_{BULK} values are generally high and consistent with an environment dominated by soil formation (≥ 80 µSI Unit). An important biological activity is attested by the abundance of earthworm diapause chambers and insect galleries filled with clay pellets and scattered mollusc shells (including large terrestrial species typical of arboreal and semi-forested environments (*Cepaea sp.*, Table 4). This biological activity is however not reflected in the organic carbon that remains low (ca. 0.1%) throughout the whole basal fluvial soil complex. Moreover, the lower part of this complex (Unit 14) underwent hydromorphic processes (lower χ_{BULK}) induced by vertical movements of the water table in the Ogosta River alluvial plain that have likely partially dissolved ferrous oxides below 19m, lowering χ_{BULK} and $\Delta\chi_{FD}$ values with respect to overlying Units 13 and 12 (Figs. 5, 7, 8C).

Given its characteristics and location regarding to the current topography of the alluvial plain, it is proposed that the basal fluvial soil complex has formed at the margins of a fluvial system that was in a similar position to the present day Ogosta River (a few meters below the base of the present day section). Indeed, the coarse sand fraction (up to 2-4 mm particles visible in the field) shows similar characteristics (grain size and mineralogy) than coarse sands sampled from the present Ogosta River

bed (grain size composition of the Ogosta river sample: silts, fine and medium sands (< 0.5mm): 20%, coarse sands (0.5-1 mm): 45% ; very coarse sands (1-2mm): 20% and fine gravels (> 2mm):15%). This observation reflects the proximity of the palaeochannel from which these sediments have been deposited through repeated flooding episodes (overbank deposits). Field and thin section observations as well as elevated redness colour index (a*), χ_{BULK} (κ_{FIELD}) and $\Delta\chi_{FD}$ all support the occurrence of soil forming processes throughout the basal fluvial soil complex. The impact of pedogenesis is also depicted in the cumulative grain size curves that show a very developed secondary mode centred around 4-5 µm (Fig. 9B). High frequency variations in both clay percentages and χ_{BULK} values through the basal fluvial soil complex suggest that the whole complex results from upbuilding soil processes (Almond and Tonkin, 1999; Eger et al., 2012) developing (aggrading) contemporaneously with repeated and variable overbank fluvial sedimentation in the alluvial plain. Sedimentological data show however that the basal fluvial soil complex is not composed of a single upbuilding soil but by a succession of at least two distinct phases.

Finally, leaching and precipitation of $CaCO_3$ at the base of the profile produced large “loess-dolls” (4-8 cm) between 19,5 and 19 meters deep (Fig. 5). The absence of strong hydromorphic imprint (no gley horizon) and the presence of terrestrial molluscs shells indicate that the soil complex originally formed on a well drained substrate and was only temporarily submerged during the strongest flooding events. According to FAO – UNESCO world reference base for soil resources (2014) these soils can be described as Bt to Bw horizons of luvic Cambisols.

Considering both soil characteristics (weathering, clay illuviation, prismatic structure) and intensity of the associated bioturbation indicating well-developed vegetation, it is proposed to assign this complex to an interglacial or interglacial/early-glacial context. According to: i) the occurrence below this complex of a periglacial sand and gravel body (T2 terrace), ii) the composition of the overlying pedosedimentary sequences and, iii) the MET-pIRIR results, and the age of the overlying tephra layer (ca. - 12 m in Fig. 5), it is proposed to allocate this part of the Harletz sequence to the upper half of MIS 7 (MIS 7c to 7a between about 220 and 190 ka, Lisiecky and Raymo, 2005) (see Section 4.2).

Finally, if it is likely according to Varga et al. (2016) or Herman et al., (2017) that a proportion of Saharan dust (20-30% of the clay) has been incorporated in interglacial soil horizons, and by using their proposed values, we could expect 7,5 to 12,5% of Saharan dust in the various units in Harletz. Although it is possible that one part of the secondary mode (2-10 microns) occurring in the grain size curves of the Harletz Soil Complex (Fig. 9B) indicates an input of Saharan dust during the Last Interglacial, such a hypothesis needs to be investigated in the future by geochemical and mineral magnetism comparisons between Harletz sediment and Saharan dust samples.

4.1.2. Loess-palaeosol sequence (LPS)

According to field observations and analytical data, the loess-palaeosol sequence of Harletz can be divided in two subsequences (Fig. 5):

1) *Subsequence 1* includes Units 11 to 2a and is composed of a thick loess body (ca. 10 m) overlain by a well developed brown soil complex (ca. 2 m),

2) *Subsequence 2* includes Units (1d to 0) and is composed of a loess complex (ca. 4 m) covered by a truncated topsoil (0 to 1.2m).

4.1.2.1. Subsequence 1: Lower loess and upper soil complex (Harletz Soil Complex)

4.1.2.1.1. Lower loess

A first break is observed in all proxy records between the top of the basal fluvial soil complex and the base of Unit 11 marking the beginning of both the loess sequence and Subsequence 1 (Fig. 5). These loess units are globally characterised by sandy facies (63-160µm: 16 to 24%), the occurrence of an important amount of carbonates (average $CaCO_3$: 15-20% excluding layers with strong secondary carbonate accumulation) and a CSI ratio of 0.6 to 1 in the lower part reaching 1 to 1.6 in the thick loess body of Unit 3a-3b. The lower part of subsequence 1 is marked by a progressive decrease over a 4m interval in clay percentages from 24-26% in the basal fluvial soil complex to 10-12% in loess at 12 m depth (Unit 4). The loss of clay content is compensated by an equivalent increase in coarse-silt

459 (25-63 µm) typical of loess deposits (Varga et al., 2012; Vandenberghe, 2013). In addition, the grain
460 size distribution spectra define a single mode characteristic of wind blown sediments, centred at 50
461 µm (Fig. 9A). Magnetic susceptibility values decline more rapidly from the top of the basal fluvial soil
462 complex, reaching average values of ca. 30 x 10^{-8} m^3/kg at the top of Unit 10, which are maintained
463 low up to the top of Unit 3b.
464 The transition between the basal fluvial soil complex and the thick loess of Unit 3 develops over a
465 depth of about 3.5 m, as a succession of four loess-soil cycles including Units 11 to 4. This part of the
466 record is characterized by the alternation of pure calcareous loess deposits, becoming progressively
467 less clayey from the base to the top (Units 11, 9, 7, 5), and of increasingly poorly developed brown to
468 grey soil horizons from the base to the top (Units 10, 8, 6, 4). These embryonic or incipient soils are
469 10 to 20 cm thick and are very well highlighted by increases in clay content (3 to 4% variation),
470 decreases in GSI, observed iron and manganese precipitates, the occurrence of pseudo-mycelium
471 (and $CaCO_3$ depletion) and of earthworm calcite granules (see Table 1). Magnetic susceptibility values
472 and its frequency dependence (Fig. 5), considered as a marker of pedogenesis, remain elevated in
473 Unit 10 which appears to be the youngest well-recorded soil horizon in this part of the sequence.
474 This soil is also indicated by a strongly bioturbated basal boundary, a granular structure, an elevated
475 clay content (25-28%), a slightly higher TOC %, and an important secondary carbonate accumulation
476 in the directly underlying loess horizon (ca. 25%).
477 Given their characteristics, and by comparison with data from Upper Last Glacial loess sequences of
478 Central Europe (Haesaerts et al., 2003, Rousseau et al., 2011), these embryonic soil horizons or
479 “rooting horizons” likely reflect short episodes of a few centuries during which wind dynamics is
480 strongly reduced allowing the development of herbaceous vegetation (steppe) in a slightly wetter
481 environment. The decrease in pedogenic intensity observed upwards from Units 10 to 4 is indicative
482 of a progressive aridification of the environment favourable to dust deflation and transport of
483 aeolian material from the surrounding environment (periglacial braided river systems) of the Danube
484 (Gabris, 1994, Gabris and Nador, 2007) and Ogosta Rivers. The cyclic alternation between loess

485 deposition and increasingly weak pedogenesis through this part of the Harletz Lower loess reveals a
486 step-by-step evolution towards more and more arid and full glacial conditions. This evolution could
487 indicate a complex transition to a Pleniglacial environment similar to what has been observed in
488 European loess sequences at the beginning of the Last Glacial period (Haesaerts and Metsdagh;
489 Antoine et al., 2016; 2000, Schirmer, 2016).
490 The exceptionally developed loess Unit 3b which shows no discontinuity in the field except for some
491 very rare and discontinuous sandy beds, corresponds to a calcareous (fine) sandy facies of loess (ca.
492 23% fine sands -63-160µm- from 12 to 7.5 m depth) characterised by very low χ_{BULK} (ca. 28 x 10^{-8}
493 m^3/kg) and $\Delta\chi_{FD}$ (< 2 x 10^{-8} m^3/kg) values over more than 4.5 m, and extremely low TOC
494 concentrations (< 0.1%) (Fig. 5). Furthermore, variations in fine sand, coarse silt and GSI co-vary
495 across Unit 3b indicating a common source for the two classes of particles. This is a typical
496 observation for sequences located near a large fluvial network (Antoine et al., 2009a, 2013). In
497 contrast, the percentage of coarse sand is close to zero between 12 and 7.5 m depth. At the
498 transition between Units 4 and 3b, the two grain size ratios (GSI and CSI) clearly show a strong shift in
499 the loess dynamics with GSI values between 1 and 1.7, corresponding to those described in other
500 typical European loess series for both Upper Weichselian (Antoine et al., 2009a,b) and Saalian loess
501 (Schirmer, 2016). In addition, within Unit 3 (6 m thick), two parts can be differentiated: a lower one
502 (12.10 to 7.4 m) showing the highest GSI and CSI values of all the sequence, and an upper one where
503 those indices gradually decrease, with an GSI passing below 1 within Unit 3a at around 7 m depth (Fig.
504 5). The detailed analysis of the grain size curves shows that the deposition of the thick loess body of
505 Units 3b and 3a was subject to high-frequency cyclical variations in grain size (mainly in fine sand and
506 coarse silt fractions that show short cycles developed over 20-30 cm in thickness). During the
507 deposition of the Harletz Lower loess, aeolian sedimentation thus was not constant resulting, more
508 likely, from successive dust storms of variable intensity as it has been proposed for the Late
509 Weichselian loess in Western Europe at Nussloch (Antoine et al., 2009a).

According to magnetic susceptibility and grain size data, the upper part of this thick loess body (Unit 3a; 7.5 to 6 m) shows evidences for weak but more and more important pedogenesis upwards. This magnetic enhancement is interpreted as resulting from a progressive climatic improvement prior to the development of the following interglacial soil (Unit 2b). The occurrence of abundant mollusc shells in the upper half of Unit 3a likely indicates a more vegetated environment during the deposition of this loess Unit than during the sedimentation of 3b in which mollusc shells are very rare. According to the observations exposed above, we proposed a subdivision of the thick loess body formed by Units 11 to 3a (total thickness of 9.9 m) into 3 sub-Units (Fig. 5), from the base to the top:

HZ-SL1 is characterised by lower sedimentation rates and the occurrence of 4 soil horizons (1 soil and 3 incipient soil horizons) showing a step-by-step evolution towards a drier and colder environment with higher sedimentation rates.

HZ-SL2 is showing a very thick and homogeneous accumulation of pure sandy calcareous loess without any weathering evidence, and the highest accumulation rates.

HZ-SL3 is characterised by a slight and progressive rise of weathering, likely a lower sedimentation rate with contemporaneous weak soil development (upbuilding) and a strong increase in mollusc populations.

4.1.2.1.2. Tephra layer at the base of HZ-SL2 sub-sequence

Although not visible during field investigations, a thin tephra layer has been evidenced by magnetic analyses at the base of Unit 3b at the contact with the incipient soil horizon of Unit 4. With respect to loess deposits in middle and lower Danube areas, tephra layers within the lower part of the second loess (thereafter L2) are reported for Serbia (Batajnica section, e.g. Markovic et al., 2009; Osipova et al., 2013; Stalac section e.g. Obreht et al., 2016), and Romania (Mostistea, e.g. Panaiotu et al., 2001; Balescu et al., 2010) (Fig. 10). There are some magnetic indications as well for a tephra in the Kaolinovo section in northeast Bulgaria (Pers. com.: Diana Jordanova). However, source assignment of this tephra layer through geochemistry is problematic as discussed in Markovic et al. (2015)

because of the strong secondary alteration of the glass shards. Taking into account the identified and MIS6 dated tephra layers in lake Ohrid sequence, a probable source of the Harletz lower loess tephra could be the Vico B-ignimbrite dated at 162 ± 8 ka from the Roman volcanic province (Leicher et al., 2016). The presence of this tephra material probably could be linked to a long-range transport at that time (ca. 950 km). In view of the lateral pattern of identified tephra in L2 loess (Markovic et al., 2015), it can be assigned to high altitude west-southwest winds.

According to the location of the tephra layer at the very base of the thick loess body of HZ-SL2 and the MET-pIRIR dates, the full loess body formed by Units 11 to 3a is allocated to the Late Saalian or MIS 6 (191-130ka). This allocation is also strongly supported by the location of this loess Unit below the first Interglacial soil (complex) occurring from the surface (Fig. 10, 11) and by luminescence ages.

4.1.2.1.3. Interglacial soil complex (Harletz Soil Complex)

At the top of the Late Saalian loess of Harletz, a thick complex (6 to 4.10 m depth) of brown to brown-greyish bioturbated palaeosols showing a strong granular structure has developed. The complex is divided into 2 Units visible in the field as well as in sedimentological and χ_{BULK} data (Units 2a-2b). The lower horizon (Unit 2b) is characterized by a gradual increase in clay percentage reaching 32-35% in its upper part. Above the limit underlined in the field by a thin and discontinuous stone line, the upper horizon (Unit 2a) shows lower clay content with values decreasing to 24-25% at its upper limit. Moreover the pedo-facies analysed both in the field and through thin sections (Fig. 6 J-L) reflects the formation of a well-developed soil: strong weathering of minerals, deep clay impregnation of the matrix, intense bioturbation (Fig. 6). The high degree of pedogenesis is also depicted by the addition of a second mode in cumulative grain size curves centred on 4-5 µm, contrasting with the unimodal distribution of unaltered loess sediments (Fig. 9B). The upper part of the Unit 2b palaeosol has then been partly eroded as evidenced by the discontinuous small stone line observed at the boundary between 2b and 2a.

561 The intense bioturbation that characterizes the palaeosol of Unit 2b, and the presence of secondary
562 $CaCO_3$ as scattered small concretions, are typical of a pedogenesis under relatively dry continental
563 and temperate climate and a forest-steppe vegetation (Phaeozems according to FAO-UNESCO, 2014).
564 The preservation of mollusc shells throughout the whole soil complex ($CaCO_3$ ≥ 15-20%) and the
565 occurrence of small calcareous concretions scattered in Unit 2a also testify for a continental climate
566 and relatively weak annual precipitation. Given the intensity of the pedogenesis revealed by the clay
567 concentrations and the very high values of magnetic susceptibility (ca. 100 x 10^{-8} m^3/kg), palaeosol 2b
568 formed under full interglacial conditions. According to its stratigraphic position, this Interglacial is
569 allocated to the Last Interglacial (MIS5e or Eemian). The ^{14}C age determination obtained from
570 mollusc shells collected at 5.65 m severely underestimates the true age likely due to the limit of the
571 radiocarbon dating method (Table 5).
572 The upper palaeosol horizon (Unit 2a), less structured than 2b and where the magnetic susceptibility
573 values and clay content decrease continuously upward, displays a vertical inverse mirror image of the
574 variation in depth of the physical properties of an in situ soil. It is thus likely that Unit 2a corresponds
575 to a slow and gradual reworking of unit 2b by colluvial processes, in a context of a relative climatic
576 degradation during which aeolian sedimentation is also active and soil formation processes weakens.
577 However, compared to the underlying soil, palaeosol 2a shows a markedly better preservation of the
578 humic matter with a TOC concentration reaching 0.4% in its middle part (by far the highest value of
579 the profile as a whole). This last point indicates an evolution of the climate towards dryer conditions
580 allowing the preservation of organic matter in the profile, which could take place during a transition
581 period (Early-glacial MIS 5-4?). Although only based on one quartz SAR age (74 ± 5 ka,) Lomax et al.
582 (2018), the geochronological control supports this idea.
583 Surprisingly, Units 2b-2a are also characterized by a high concentration of coarse sands (5-7%)
584 significantly anti-correlated with the fine sands (Fig. 5). These coarse sands are easily visible when
585 conducting wet sieving tests of malacological samples over a 500µm mesh. The mineralogy and
586 grain-size of the coarse sand are similar to that of present-day sands collected from the Ogosta River

bed (see above). This suggests that an additional proximal source (tens to hundreds of meters) was active during the deposition of loess sediments on which developed the interglacial palaeosol 2b (see section 4.2 for further discussion).

4.1.2.2. Subsequence 2: Upper loess and topsoil.

In the field, the upper part of the sequence of Harletz (Units 1d-1a) shows a particularly monotonous record, partly due to strong desiccation even though the section face was excavated one meter or more inwards. Contrastingly, sedimentological analyses, magnetic properties and colour reflectance show significant variations, strongly correlated with each other (Fig. 5).

Two horizons with low degree of pedogenesis are thus evidenced within the loess Unit 1. The first horizon, within Unit 1c, ranges between 3 to 2 m depth (relative variation of clay content: 7%). The second horizon, within Unit 1b, from 2 to 1.5 m depth, is thinner and shows a lower degree of alteration (relative variation of the clay content: 2-3%). These observations are important for the interpretation of the sequence because they indicate that the upper 4 m of loess of Unit 1, although thinner than the loess Unit 3, does not necessarily correspond to a shorter phase of deposition. On the contrary, they rather correspond to a complex and long climate history corresponding to a succession of stadial and interstadial phases. The stadial phases are characterized by maximum GSI values and minima in magnetic susceptibility, clay content and a* values.

OSL and ^{14}C ages allow to allocate this part of the profile to the Last Glacial period (Weichselian) indicating a very low sedimentation rate for this period (4m / 60-50 ka). This results in smoothed variation in the various analytical data, mimicking the variations of the LR-04 global stack for deep-sea records (Lisiecki and Raymo, 2005) in accordance with the chronological interpretation proposed above (Fig. 11). According to this interpretation, the horizons showing weak pedogenesis in Units 1c and 1b, correspond to loess deposited during the Middle Pleniglacial (mainly MIS 3) in a particularly arid environment and unfavourable to soil development as compared with Serbian profiles (Antoine

et al., 2009b). The results of the OSL (Table 3) and ^{14}C age determinations (Table 5) are consistent with this interpretation.

Finally, if the topsoil has been eroded at the main profile, a lateral section located 30 m to the Northeast allowed to describe a more complete profile, 1.5 m thick including a typical humic horizon of chernozem with a strongly bioturbated lower boundary (rodent burrows, earthworm tubules) and a calcium carbonate horizon (not described in this paper).

4.2 Correlations and regional significance of the record

Using a cyclo-stratigraphic approach of the sequence combined with dating constraints provided by both luminescence ages and the occurrence of the tephra layer at 12 meter depth, the Harletz section exhibits a remarkably high-resolution Late Saalian (MIS6) loess accumulation in Europe (L2 loess) (Fig. 10). Indeed, if similar values have been reported from the Serbian sequences of the Titel Plateau area (8.2m, Markovic et al., 2015), from the Koriten core of NE Bulgaria (7 m, Jordanova et al., 2007) or in some west European profiles as at Kesselt in Belgium (7-8m, Meijs, 2002) or Achenheim in France (ca. 8m, Lautridou et al., 1985), other Danubian profiles, especially in Romania, show a markedly lesser L2 thickness (4.5 to 6m including an interstadial soil in the lower part) (Fig. 10).

Looking for regional references for the basal fluvial soil complex (Ogosta Soil Complex), the closest and best-dated high-resolution palaeoenvironmental archive is the Lake Ohrid record located at 400 km to the SW of Harletz (Sadori et al., 2016, Francke et al., 2016). In this reference record, MIS 7 corresponds to the upper part of palynozone OD-6 characterised by an alternation of coniferous and mesophylous forests with grassland (steppe) formations (Sadori et al., 2016); a vegetation which is in good accordance with the pedological signature of the basal soil complex at Harletz. The BFS complex developed in an alluvial plain environment from a parent material that is not loess, inducing a difference in soil facies with respect to contemporaneous S2 soil complexes occurring below L2 Late Saalian loess in regional records along the Danube from Serbia to the Romanian coast or to the Late Saalian loess of Western Europe (Fig. 10). In all the Danubian loess sections the S2 soil is described as

638 a typical chernozem soil. In Harletz, the basal fluvial soil complex characteristics are more typical of a
639 leached Cambisol indicating a riparian environment: more humid conditions and a forested
640 landscape in accordance with its location within the Ogosta River alluvial plain, where trees or shrubs
641 likely grew during MIS 7 (molluscs from forested environments), in contrast to slopes and plateaux
642 covered by steppe vegetation, as today.
643 Overlying the Ogosta Soil Complex, the lower part of L2 loess includes an exceptionally detailed
644 succession of loess and incipient soil horizons never described in European loess until now. The basal
645 sequence of L2, denoted HZ-SL1, is very important as it testifies of a progressive step-by-step
646 evolution of climate and of the environment during the transition between MIS 7 and MIS6 (Fig. 11).
647 In Lake Ohrid reference pollen record, this transitional phase likely corresponds to palynozone OD5
648 between 190 and 160 ka (Sadori et al. 2016) characterised by a grassland-dominated environment
649 (*Poaceae* and *Cyperaceae*). During this phase, a succession of 3 to 4 short (millennial) interstadial
650 phases have been evidenced between 190 and 170 ka by both strong increases in mesophylous
651 species (Sadori et al., 2016) and peaks in the TOC records (Francke et al., 2016). It is likely that they
652 correspond to the succession represented by the soil of Unit 10 and incipient soils of Units 8, 6 and 4
653 in the Harletz loess record (Fig. 12). Global climate records, such as the deep-sea LR-04 global $\delta^{18}O$
654 records (Lisiecky and Raymo, 2005, Railsback, et al., 2015), are not very contrasted over MIS 6.
655 However, high-resolution $\delta^{18}O$ (*G. bulloides*) records from the Iberian margin (Hodel et al., 2013),
656 provide evidence for a succession of short interstadial episodes spreading between about 190 and
657 165 ka that could be concomitant with the Harletz incipient soil horizons (units 8, 6 and 4 in Fig. 12).
658 The extremely cold and arid period of MIS 6 seems thus to last about 30 ka (≈ 170-140 ka) in both
659 Lake Ohrid, Harletz loess-palaeosol sequence, and Iberian margin marine records.
660 During the younger part of MIS6 (160-129ka), steppe vegetation with overwhelming herbs
661 (*Artemisia*) is dominant (Sadori et al., 2016). This time interval (OD4 Zone) is characterized by the
662 driest conditions observed in the 500 ka record of lake Ohrid and very similar vegetation history
663 during this period is observed also in the pollen record from Tenaghi Phillipon in Greece (Tzedakis et

al., 2003, 2006). This is in good accordance with a global enhancement of aeolian dynamics recorded in almost all the European loess section at that time (Fig. 10). It is especially the case in sections located close to the Danube River from Serbia to Bulgaria and Romania where L2 loess (MIS 6) always appears as the thickest loess interval of the entire loess-palaeosol record (Fig. 10). Even if during the last 200 ka, MIS 6 is considered as a very cold period it is not so different from MIS 2 in terms of ice volume and global climatic conditions, and the difference in aeolian sedimentary budgets could more likely result from a markedly longer period favourable to dust deflation during MIS 6 (ca. 35 ka) than during MIS 4+2 (ca. 25 ka).

The strong increase in loess sedimentation rates during MIS 6 is also recorded in Western Europe, for example, in Northern France (Antoine, et al., 2015, Hérisson et al., 2016), Belgium (Juvigné et al., 1996; Vandenberghe et al., 1998; Meijs, 2002, 2011) or in Germany (Lehmkuhl et al., 2016). In Western Europe, late MIS 6 includes finely laminated loess facies with micro-frost cracks resulting from niveo-aeolian processes indicating a relatively important snow cover. This loess body is interrupted by up to five tundra gley horizons (15-20 cm thick) connected to large ice wedge casts networks (Meijs, 2000, Vandenberghe et al., 1998) testifying for ice-rich permafrost and markedly more humid conditions (snow cover) than in South-East Europe (Fig. 10).

However, even if the global context is very cold, lower aeolian dynamics and a sharp increase in biodiversity (molluscs) both characterize MIS 6 tundra gley horizons, as those from the Late Weichselian (Antoine et al., 2009a). This indicates that short (millennial) climatic oscillations had an impact on Western Europe during the lower half of the Late Saalian (Vandenberghe et al., 1998). Though these Western European Late Saalian loess sequences lack accurate age determinations, the similarity of their pedosedimentary succession with those from SE Europe loess allow to correlate tundra gley horizons of Western Europe to incipient soils at Harletz. This comparison seems to show that millennial climatic variability is recorded in aeolian sequences all over Europe, not only during the Last glacial period, but also during the Penultimate glacial period. Finally, this episode characterised by high loess sedimentation rates in Europe corresponds to a global feature, which is

690 contemporaneous of a strong maximum in dust concentrations in the EPICA Dome C record (Lambert
691 et al., 2008).
692 At Harletz, the later stage of MIS 6 loess accumulation (subsequence HZ-SL3) shows a weakly
693 weathered facies compared to the underlying pure sandy loess, indicating a progressive warming
694 trend that is also well depicted in the Lake Ohrid record in the Upper part of OD-4 (138-128ka) during
695 which the mesophylous species show a progressive increase to Interglacial values. This evolution
696 seems to be characteristic of the upper part of L2 in the Lower Danube region suggesting that aeolian
697 sedimentation strongly reduced but remained active during the transition to the Eemian and perhaps
698 even during the interglacial itself. This contrasts with western European sections, where aeolian
699 sedimentation clearly stops before the development of a down-building Interglacial brown leached
700 soil, which overprints the previously decalcified loess.
701
702 **4.3. Loess and sand sources, palaeo-wind implications**
703 In the lower Danube area, during glacial times, the main source of silt and fine sands for loess
704 deposition is the Danube braided alluvial plain. This is supported by observed variations in sequence
705 thickness, average grain-size, and distance from the Danube River (Jipa, 2014). Past wind directions
706 have been reconstructed based on morphological constraints (Greda orientations: Rozycki, 1967) and
707 grains size gradients relative to a Danubian source (Evlogiev, 2007, Jipa, 2014). Dominant wind
708 directions are NW to W-NW in the middle and upper part of the Lower Danube, and N-NW to N
709 directions when approaching the Black Sea (Fig. 1B). This pattern likely results from the deviation of
710 the main winds by the Carpathian Mountains.
711 According to these interpretations, the silts and fine sands building the Harletz loess section would
712 have been transported from the Danube braided river system located (at that time) about 4.5 km to
713 the NW (Fig. 13A). The occurrence of high W-E to NW-SE elongated loess ridges (gredas), only on the
714 right bank of the Ogosta River, is in accordance with the implied wind directions and indicate
715 formation of gredas from Ogosta River sediments transported by west-northwest winds (Fig. 13A).

716 Based on our data, the main loess units, and especially Unit 3a, are characterised by a very low to a
717 total absence of coarse sand particles (Fig. 5 and Table 2). According to the position of the section
718 regarding the very close Ogosta alluvial plain, this observation implies that strong wind able to
719 transport coarse sand grains (up to 2-3 mm) were not blowing from the East or Northeast during the
720 Late Saalian. In addition, Saalian loess are characterised by a high proportion of fine sands (22-25% in
721 the thick Unit 3a, Fig. 5). According to the absence of coarse particles originating from the Ogosta
722 valley in Units 3a-3b, these fine sands (and coarse silts), which form the main component of Unit 3,
723 were likely transported from Danube sources during northwestern storm events by saltation over
724 about 4.5 km and over important topography separating the Danube Valley from the Harletz section
725 (ca. 40 m in elevation at the base of the Harletz section, Fig. 13B). A similar case has been
726 demonstrated for the Last Glacial in the Rhine River at Nussloch, where important amounts of fine
727 sands deflated from the braided Rhine River have been transported (drifted) on the eastern slope
728 and deposited on the plateau located at 3 km and 100 m above from the source by NW storms
729 (Antoine et al., 2001).
730 However, given the position of the studied section relative to the periglacial plain of the Ogosta River,
731 one might expect that the Ogosta River alluvial plain was the major source of detrital material during
732 glacial times. However, the analysis of sands sampled from the sandy-gravelly bottom of the current
733 river shows that they are very rich in coarse sand grains and very fine gravels not observed in the
734 loess of Unit 3. However, coarse sand percentages are the highest in the Harletz Soil Complex (Unit
735 2a-b, Fig. 5). As the percentage of coarse sands has been calculated independently of the other
736 fractions (mass of grains > 160 um / total mass of the sample), and also checked by the classical
737 sieving method (Table 1 and red dots in Fig. 5), this result is not an artefact resulting from variations
738 in the relative proportions of the fine and coarse sand components (Fig. 5). Taking into account this
739 observation, it is clear that dominant wind regimes and thus climatic configurations have not been
740 constant during the sedimentation of the Harletz sequence. It is therefore proposed that (Fig. 13):

741 1) during full glacial times, silts and fine sands accumulating to form the main loess units were
742 transported from the braided river system of the Danube River during storm events blowing from W-
743 NW. At that time, the topographic step between the steep slope of the left bank of the Ogosta valley
744 and the alluvial plain produced a sediment trap allowing the downwind preservation of a thick loess
745 sequence (Fig. 3). During full glacial times, the intensity of easterly-northeast winds is likely
746 insufficient to transport coarse sand particles from the Ogosta River plain to the Harletz site.
747 2) During the Eemian interglacial, and to a lesser extent during interstadials, long distance transport
748 of silt and fine sand particles characteristic of glacial periods is stopped but weak aeolian
749 sedimentation is driven by north-easterly winds transporting coarse sand grains from the very
750 proximal sandy banks of the Ogosta River on the ramp previously shaped during glacial loess
751 deposition.
752 3) Finally, the contrast between the thick Saalian accumulation and the thinner Last Glacial loess is
753 likely linked to a change in topographical setting. The sediment trap favouring thick accumulation
754 during the Saalian was rapidly filled during the Last Glacial enabling continued down wind transport.
755 Since the Early Holocene, strong anthropogenic erosion in upper part of the sequence is also
756 evidenced.
757 Finally, to interpret the absence of coarse sand grains in the whole Harletz loess deposits (especially
758 during MIS6), without involving a change in wind directions, we could propose another hypothesis
759 involving a change in the availability of coarse particles from the Ogosta River between glacial and
760 interglacial times:
761 1) During glacial periods the development of a steppe in the Ogosta alluvial plain inhibits the
762 transportation (saltation) of coarse particles to the valley slopes.
763 2) At the opposite, during Interglacial periods the Ogosta River is characterised by a meandering
764 system with large non vegetated sandy river banks exposed to deflation by NE winds and able to
765 provide coarse sand grains during stormy events.
766

5. Conclusions

The multi-disciplinary approach and high-resolution investigations and luminescence dating undertaken on the 20 m high Harletz loess-palaeosol section, coupled with a correlation with other European loess and lacustrine reference records led to the following conclusions:

1) The lower 4 m of the profile are represented by an upbuilding brown soil complex (Ogosta Soil Complex) developed on alluvial silty sands deposited in the Ogosta River alluvial plain during an interglacial period that can be allocated to MIS 7.
2) The Harletz profile then exhibits a 10 m thick Late Saalian (MIS 6) loess accumulation that, until present, is remarkable in Europe.
3) The lower part of the main loess accumulation (HZ-SL1) includes an exceptionally thick (4 m) and detailed cyclic succession of four loess and four incipient soil horizons never described previously in European loess. This part of the record testifies of a progressive step-by-step evolution in the climate and in the environment during the transition from MIS 7 to MIS 6 and correlates well with the palynological record of Lake Ohrid (Sadori et al., 2016).
4) During the younger part of MIS 6 (160-129 ka), a global enhancement of the aeolian dynamics is evidenced during a period characterised by steppe vegetation with overwhelming herbs (*Artemisia*) in the Lake Ohrid record. This period is especially well recorded in sections located close to the Danube River from Serbia to Bulgaria and Romania (HZ-SL2 / L2 loess).
5) The tephra occurring at 12 m depth within MIS 6 loess (HZ-SL2) represents an important element of comparison with sections in Romania and Serbia where a tephra was reported in the same stratigraphic position at the base of loess L2 at about 170-160 ka.
6) According to grain size and topographic data, silts and fine sands building the Harletz loess section during glacial periods would have been transported from the Danube braided river system located at that time at ca. 4.5 km to the NW. By contrast, during the Eemian interglacial, and to a lesser extent during MIS 5 and 3 interstadials, the long distance

transport of silt and fine sand particles is stopped and a weak aeolian sedimentation is likely driven by north-easterly winds transporting coarse sand grains from the proximal sandy banks of the Ogosta River.

7) Finally, from a geomorphological point of view, this work provides geochronological constraints for the T2 terrace, allocating its formation to the cold stage directly preceding MIS 7 or MIS 8.

Data Availability

The multi-proxy data sets presented in the present article will be made available on the Pangea data repository (https://www.pangaea.de/) once accepted.

Acknowledgments

This study benefited from research funds granted by the ANR to DDR (ACTES project ANR-08-BLAN-0227 - CSD 6), the CNRS-INSU SYSTER program to FL (2012-31124A) and the PHC Rila program to FL and DJ (34286QB). This is IPGP contribution n° XXX and LDEO contribution 8271

References

Almond, P. C., and Tonkin P.J., 1999. Pedogenesis by upbuilding in an extreme leaching and weathering environment, and slow loess accretion, south Westland, New Zealand. Geoderma, 92, 1-36.

Antoine, P., Rousseau, D.-D., Zöller, L., Lang, A., Munaut, A.-V., Hatté, C., Fontugne, M., 2001. High-resolution record of the last Interglacial-glacial cycle in the Nussloch loess-paleosol sequences, Upper Rhine Area, Germany. Quaternary International 76-77, 211-229.

Antoine, P., Rousseau, D.-D., Moine, O., Kunesch, S., Hatté, C., Lang, A., Tissoux, H., Zöller, L., 2009a. Rapid and cyclic aeolian deposition during the Last Glacial in European loess: a high-resolution record from Nussloch, Germany. Quaternary Science Reviews 28, 2955-2973.

819 Antoine, P., Rousseau, D.D, Fuchs, M., Hatté, C., Marcovic, S.B., Jovanovic, M., Gaudenyi, T., Moine,
820 O., Rossignol, J. 2009b. High resolution record of the Last Climatic Cycle in the Southern
821 Carpathian basin at Surduk (Vojvodina, Serbia). Quaternary International 198, 19-36.
822 Antoine, P., Rousseau, D.-D., Degeai, J.-P., Moine, O., Lagroix, F., Kreutzer, S., Fuchs, M., Hatté, C.,
823 Gauthier, A., Svoboda, J., Lisà, L., 2013. High-resolution record of the environmental response to
824 climatic variations during the Last Interglacial–Glacial cycle in Central Europe: the loess-
825 palaeosol sequence of Dolní Věstonice (Czech Republic). Quaternary Science Reviews 67, 17-38.
826 Antoine, P., Limondin-Lozouet, N., Auguste, P., Locht, J.-L., Debenham, N., Bahain J.-J., Goval., E.,
827 Fagnart, J.P., and Ducrocq, T. 2015. Quaternary geoarchaeology and prehistory: The model of
828 the Somme valley (France) and the neighbouring regions In *: Arnaud-Fassetta G. and Carcaud N.*
829 *eds*. French geoarchaeology in the 21st century, CNRS éditions, 71-86.
830 Antoine, P., Coutard, S., Guérin, G., Deschodt, L., Goval, E., Locht, J.-L., Paris, C., 2016. Upper
831 Pleistocene loess-palaeosols records from Northern France in the European context:
832 environmental background and dating of the Middle Palaeolithic. Quaternary International 411,
833 4-24.
834 Avramov, V. I., Jordanova, D., Hoffmann, V., Roesler, W., 2006. The role of dust source area and
835 pedogenesis in three loess-palaeosol sections from North Bulgaria: A mineral magnetic study.
836 Quaternary-International, Studia Geophysica et Geodaetica, Springer, 50, 259-282.
837 Balescu, S., Lamothe, M., Panaiotu, C. and Panaiotu, C. 2010. La chronologie IRSL des séquences
838 loessiques de l'est de la Roumanie. Quaternaire 21(2), 115-126.
839 Balsam, W.L., Ellwood, B.B., Ji, J.F., Williams, E.R., Long, X.Y. and El Hassani, A., 2011. Magnetic
840 susceptibility as a proxy for rainfall: Worldwide data from tropical and temperate climate.
841 Quaternary Science Reviews, 30(19-20): 2732-2744.
842 Boch, R., Cheng, H., Spötl, C., Edwards, R.L., Wang, X., Häuselmann, P., 2011. NALPS: a precisely
843 dated European climate record 120–60 ka. Climate of the Past 7, 1247-1259.

844 Barker, S., Knorr, G., Edwards, L., Parrenin, F., Putnam, A. E., Skinner, L. C., Wolff, E., Ziegler, M. 201.
845 800,000 Years of Abrupt Climate Variability. Science 334, 347-351.
846 Baumgarten, H., Wonik, T., Tanner, D. C., Francke, A., Wagner, B., Zanchetta, G., Sulpizio, R., B.
847 Giaccio, B. and Nomade, S. 2015. Age-depth model of the past 630 kyr for Lake Ohrid
848 (FYROM/Albania) based on cyclostratigraphic analysis of downhole gamma ray data.
849 Biogeosciences, 12, 7453-7465.
850 Cottereau, E., Arnold, M., Moreau, C., Baqué, D., Bavay, D., Caffy, I., Comby, C., Dumoulin, J.-P., Hain,
851 S., Perron, M., Salomon, J., Setti 2007. Artemis, the New ^{14}C AMS at LMC14 in Saclay, France
852 Radiocarbon 49, 291–299.
853 Dearing, J.A., Bird, P.M., Dann, R.J.L., and Benjamin, S.F., 1997. Secondary ferrimagnetic minerals in
854 Welsh soils: a comparison of mineral magnetic detection methods and implications for mineral
855 formation. Geophysical Journal International, 130(3), 727-736.
856 Debret, M., Sebag, D., Desmet, M., Balsam, W., Copard, Y., Mourier, B., Susperrigui, A. S., Arnaud, F.,
857 Bentaleb, I., Chapron, E., Lallier-Verges, E., and Winiarski, T. 2011. Spectrocolorimetric
858 interpretation of sedimentary dynamics: The new “Q7/4 diagram”, Earth-Rev. Rev., 109, 1–19.
859 Desprat, S., Sánchez-Goñi, M.F., Naughton, F., Turon, J.-L., Duprat, J., Malaizé, B., Peypouquet, J.-P.,
860 2007. Climate variability of the last five isotopic interglacials: Direct land-sea-ice correlation
861 from the multiproxy analysis of North-Western Iberian margin deep-sea cores, In: Sirocko, F.,
862 Claussen, M., Sánchez Goñi, M.F., Litt, T. (Eds.), The climate of past interglacials. Elsevier,
863 Amsterdam, pp. 375-386.
864 Eger, A., Almond, P.C., and Condron, L.M. 2012. Upbuilding pedogenesis under active loess
865 deposition in a super-humid, temperate climate-quantification of deposition rates, soil
866 chemistry and pedogenic thresholds. Geoderma 189-190, 491-501.
867 Ehrmann, W., Schmiedl, G., Beuscher, S., Krüger, S., 2017. Intensity of African Humid Periods
868 Estimated from Saharan Dust Fluxes. PLoS ONE 12(1): e0170989.
869 https://doi.org/10.1371/journal.pone.0170989.

870 Evlogiev, Y., 2007. Evidence for the Aeolian Origin of Loess in the Danubian Plain. Geologica
871 Balkanica, 36 (3-4), 31-39.
872 Evlogiev, Y., 2015 In: Environment impact assessment report on investment proposal “construction
873 of national disposal facility for low and intermediate level radioactive waste – ndf” - part iii.
874 2015, Sofia, p. 98.
875 Evstatiev, D., Angelova, R. and Evlogiev, Y. 2000. Characteristics of loess as host media for radioactive
876 waste disposal. In : 8th International IAEG Congress. Balkema, Rotterdam, 4537-4544.
877 Eyre, J. K. 1997. Frequency dependence of magnetic susceptibility for populations of single-domain
878 grains. Geophysical Journal International 129, 209-211.
879 FAO UNESCO 2014. World Soil Resources Report 106, World reference base for soil resources 2014
880 International soil classification system for naming soils and creating legends for soil maps,
881 Update 2015. 192p.
882 Francke, A., Wagner, B., Just, J., Leicher, N., Gromig, R., Baumgarten, H., Vogel, H., Lacey, J. H., Sadori,
883 L., Wonik, T., Leng, M. J., Zanchetta, G., Sulpizio, R., and Giaccio, B. 2016. Sedimentological
884 processes and environmental variability at Lake Ohrid (Macedonia, Albania) between 637 ka and
885 the present, Biogeosciences, 13, 1179–1196, doi:10.5194/bg-13-1179-2016, 2016.
886 Fuchs, M., Rousseau, D.D., Antoine, P., Hatté, C. and Gauthier C. 2007. Chronology of the Last
887 Climatic Cycle (Upper Pleistocene) of the Surduk loess sequence, Vojvodina, Serbia. Boreas 10,
888 1-8.
889 Fuchs, M., Kreutzer, S., Rousseau, D.D., Antoine, P., Hatté, C., Lagroix, F., Moine, O., Gauthier, C.,
890 Svoboda, J., Lisá, L. 2013. The loess sequence of Dolni Vestonice (Czech Republic): a new OSL
891 based chronology of the Last Climatic Cycle. Boreas 42, 664-677.
892 Fotakieva, E. and Minkov, M. 1966. Der Löß in Bulgarien. Eiszeitalter und Gegenwart 17, 87-96.
893 Gabris, G. 1994. Pleistocene evolution of the Danube in the Carpathian Basin. Terra Nova 6, 495-501.

894 Gabris, G., and Nador, A. 2007. Long-term fluvial archives in Hungary: response of the Danube and
895 Tisza rivers to tectonic movements and climatic changes during the Quaternary: a review and
896 new synthesis. Quaternary Science Reviews 26 (22-24), 2758-2782.
897 Giosan, L., Coolen, M.J.L., Kaplan, J.O., Constantinescu, S., Filip, F., Filipova-Marinova, M., Kettner,
898 A.J., and Thom, N. 2012. Early Anthropogenic Transformation of the Danube-Black Sea System.
899 Scientific Reports, 2 : 582 | DOI: 10.1038/srep00582.
900 Gauthier, C. and Hatté, C. (2008) Effects of handling, storage, and chemical treatments on $\delta^{13}C$ values
901 of terrestrial fossil organic matter. Geophysics, Geochemistry and Geosystem 9(8), doi:
902 10.1029/2008GC001967.
903 Gocke, M., Hambach, U., Eckmeier, E., Schwark, L., Zöller, L., Fuchs, M., Löscher, M., Wiesenberg,
904 G.L.B. 2014. Introducing an improved multi-proxy approach for paleoenvironmental
905 reconstruction of loess-paleosol archives applied on the Late Pleistocene Nussloch sequence
906 (SW Germany). Palaeogeography, Palaeoclimatology, Palaeoecology 410, 300-315.
907 Haase, D., Fink, J., Haase, G., Ruske, R., Pécsi, M., Richter, H., Altermann, M., Jäger, K-D., 2007. Loess
908 in Europe - its spatial distribution based on a European Loess Map, 1:2 500 000. Quaternary
909 Science Reviews 26, 1301-1312.
910 Haesaerts, P. and Metsdagh, H., 2000 - Pedosedimentary evolution of the last interglacial and early
911 glacial sequence in the European loess belt from Belgium to central Russia, Geologie en
912 Mijnbouw, 79(2-3), 313-324.
913 Haesaerts, P., Borziak, I., Chirica, V., Damblon, F., Koulakovska, L., van der Plicht, J., 2003. The East
914 Carpathian loess record: a reference for the Middle and Late Pleniglacial stratigraphy in Central
915 Europe. Quaternaire 14, 163-188.
916 Haesaerts, P., Damblon, F., Gerasimenko, N., Spagna, P., Pirson, S., 2016. The Late Pleistocene loess-
917 palaeosol sequence of Middle Belgium. Quaternary International 411, 25-43.
918 Hatté, C., Fontugne, M., Rousseau, D.-D., Antoine, P., Zöller, L., Tisnérat-Laborde, N., Bentaleb, I.,
919 1998. $d^{13}C$ variations of loess organic matter as a record of the vegetation response to climatic

changes during the Weichselian. Geology 26, 583-586.

Heiri, O., Koinig, K.A., Spötl, C., Barrett, S., Brauer, A., Drescher-Schneider, R., Gaar, D., Ivy-Ochs, S., Kerschner, H., Luetscher, M., Moran, A., Nicolussi, K., Preusser, F., Schmidt, R., Schoeneich, P., Schwörer, C., Sprafke, T., Terhorst, B., Tinner, W., 2014. Palaeoclimate records 60–8 ka in the Austrian and Swiss Alps and their forelands. Quaternary Science Reviews 106, 186-205.

Hérisson, D., Coutard, S., Goval, E., Locht, J.-L., Antoine, P., Chantreau,Y., Debenham, N. 2016. A new key-site for the end of the Lower Palaeolithic and the onset of the Middle Palaeolithic at Etricourt-Manancourt (Somme, France). Quaternary International 409(B), 73-91.

Hodell, D., Crowhurst, S., Skinner, L., Tzedakis, P. C., Margari, V., Channell, J.E.T., Kamenov, G., Maclachlan, S., Rothwell, G. 2013. Response of Iberian Margin sediments to orbital and suborbital forcing over the past 420 ka. Paleocenography. 28. 185-199. 10.1002/palo.20017.

Hošek, J., Hambach, U., Lisá, L., Matys Grygar, T., Horáček, I., Meszner, S., Knésl, I. 2015. An integrated rock-magnetic and geochemical approach to loess/paleosol sequences from Bohemia and Moravia (Czech Republic): Implications for the Upper Pleistocene paleoenvironment in central Europe. Palaeogeography, Palaeoclimatology, Palaeoecology 418, 344-358.

Ji, J.F., Chen, J., Balsam, W., Lu, H.Y., Sun, Y.B., Xu, H.F., 2004. High resolution hematite/goethite records from Chinese loess sequences for the last glacial–interglacial cycle: rapid climatic response of the East Asian Monsoon to the tropical Pacific. Geophysical Research Letters 31.

Jipa, D.C., 2014. The loess-like deposits in the Lower Danube basin. Genetic significance. Geo-Eco-Marina, 20, 7-18.

Jordanova, D., Petersen, N., 1999. Palaeoclimatic record from a loess-soil profile in northeastern Bulgaria. I. Rock magnetic properties. Geophysical Journal International, 138, 520-532.

Jordanova, D., Hus, J., Geeraerts, R., 2007. Palaeoclimatic implications of the magnetic record from loess/palaeosol sequence Viatovo (NE Bulgaria). Geophysical Journal International 171, 1036-1047.

946 Jordanova, D., Hus, J., Evlogiev, J., Geeraerts, R., 2008. Palaeomagnetism of the loess/palaeosol
947 sequence in Viatovo (NE Bulgaria) in the Danube basin. Physics of The Earth and Planetary
948 Interiors 167, 71-83.
949 Juvigné, E., Haesaerts, P., Metsdagh, H., Balescu, S. 1996. Révision du stratotype loessique de Kesselt
950 (Limbourg, Belgique). Compte Rendu de l'Académie des Sciences, Paris, série IIa, 323, 801-807.
951 Konert, M. and Vandenberghe, J. 1997. Comparison of laser grain size analysis with pipette and sieve
952 analysis: a solution for the underestimation of the clay fraction. Sedimentology 44, 523-535.
953 Kukla, G. 1977. Pleistocene land-sea correlations. 1: Europe. Earth-Science Reviews 13, 307–374.
954 Lambert, F., Delmonte, B., Petit, J.R., Bigler, M., Kaufmann, P. R., and Hutterli, M.A., Stocker, T.F.,
955 Ruth, U., Steffensen, J. P., Maggi, V.. 2008. Dust - Climate couplings over the past 800,000 years
956 from the EPICA Dome C ice core. Nature 452. 616-9. 10.1038/nature06763.
957 Lautridou, J.-P., Sommé, J., Heim, J., Puisségur, J.-J., et Rousseau, D.-D., 1985. La stratigraphie des
958 loess et formations fluviatiles d'Achenheim (Alsace): nouvelles données bioclimatiques et
959 corrélations avec les séquences pléistocènes de la France du Nord-Ouest. Bulletin de
960 l'Association Française pour l'Etude du Quaternaire 22, 125-132.
961 Lehmkuhl, F., Zens, J., Krauß, L., Schulte, P., Kels, H., 2016. Loess-paleosol sequences at the northern
962 European loess belt in Germany: Distribution, geomorphology and stratigraphy. Quaternary
963 Science Reviews 153, 11-30.
964 Leicher, N., Zanchetta, G., Sulpizio, R., Giaccio, B., Wagner, B., Nomade, S., Francke, A., Del Carlo, P.,
965 2016. First tephrostratigraphic results of the DEEP site record from Lake Ohrid (Macedonia and
966 Albania). Biogeosciences 13, 2151–2178.
967 Li, B. and Li, S.-H., 2011. Luminescence dating of K-feldspar from sediments: A protocol without
968 anomalous fading correction. Quaternary Geochronology 6 (5), 468–479.
969 Lisiecki, L.E., Raymo, M.E., 2005. A Pliocene-Pleistocene stack of 57 globally distributed benthic $\delta^{18}O$
970 records. Paleoceanography 20, PA 1003.

971 Luetscher, M., Boch, R., Sodemann, H., Spötl, C., Cheng, H., Edwards, R. L., Frisia, S., Hof, F., and
972 Müller, W. 2015. North Atlantic storm track changes during the Last Glacial Maximum recorded
973 by Alpine speleothems. Nature Communication 6, 1-6.
974 Lomax, J., Fuchs, M., Preusser, F.; Fiebig, M. 2014a. Luminescence based loess chronostratigraphy of
975 the Upper Palaeolithic site Krems-Wachtberg, Austria. Quaternary International 351, 88-97.
976 Lomax, J., Kreutzer, S., Fuchs, M. 2014b. Performance tests using the Lexsyg luminescence reader.
977 Geochronometria 41 (4).
978 Lomax, J., Fuchs, M., Antoine, P., Rousseau, D.-D., Lagroix, F., Hatté, D., Taylor, S., Till, J., Debret, M.,
979 Moine, O., Jordanova, D. 2018. A luminescence-based chronology for the Harletz loess sequence,
980 Bulgaria. Boreas. https://doi.org/10.1111/bor.12348.
981 Maher, B.A. and Taylor, R.M., 1988. Formation of ultrafine-grained magnetite in soils. Nature, 336:
982 368-371.
983 Margari, V., Skinner, L.C., Tzedakis, P.C., Ganopolski, A., Vautravers, M. and Shackleton, N.J., 2010.
984 The nature of millennial-scale climate variability during the past two glacial periods. Nature
985 Geoscience 3, 127-131.
986 Marković, S.B., Hambach, U., Catto, N., Jovanović, M., Buggle, B., Machalett, B., Zöller, L., Glaser, B.,
987 Frechen, M., 2009. The middle and late Pleistocene loess–paleosol sequences at Batajanica,
988 Vojvodina, Serbia. Quaternary International 198, 255–266.
989 Marković, S.B., Stevens, T., Kukla G.J., Hambach, U., Fitzsimmons, K.E., Gibbard, P., Buggle, B., Zech,
990 M., Guo, Z., Hau, Q., O'Hara, Dhand K., Smalley, I., Újvári, G., Sümegi, P., Timar-Gabor, A., Veres,
991 D., Sirocko, F., Jary, Z, Svensson, A., Jović, V., Kovács, J., Zvirčev, Z., Vasiljević, D.A. 2015. The
992 Danube loess stratigraphy – new steps towards a pan-European loess stratigraphic model. Earth
993 Science Reviews 148, 228-258.
994 Martrat, B., Grimalt, J.O., Lopez-Martinez, C., Cacho, I., Sierro, F.J., Flores, J.A., Zahn, R., Canals, M.,
995 Curtis, J.H., Hodell, D.A. 2004. Abrupt Temperature Changes in the Western Mediterranean over
996 the Past 250,000 Years. Science 306, 1762-1765.

997 Martrat, B., Grimalt, J.O., Shackleton, N.J., de Abreu, L., Hutterli, M.A. and Stocker, T.F., 2007. Four
998 climate cycles of recurring deep and surface water destabilizations on the Iberian Margin,
999 Science 317, 502-507.
1000 Meijs, E.P.M., 2002. Loess stratigraphy in Dutch and Belgian Limburg. Eiszeitalter und Gegenwart 51,
1001 114-130.
1002 Meijs, E.P.M., 2011. The Veldwezelt site (province of Limburg, Belgium): Environmental and
1003 stratigraphical interpretations. Netherlands Journal of Geosciences, Geologie en Mijnbouw 90,
1004 73-94.
1005 Moine, O., Rousseau, D.-D., Antoine, P. and Hatté, C. 2002. Mise en évidence d'événements
1006 climatiques rapides par les faunes de mollusques terrestres des loess weichseliens de Nussloch
1007 (Allemagne). Quaternaire 13 (3-4), 209-218.
1008 Moine, O., Rousseau, D.-D., Antoine, P., 2008. The impact of Dansgaard-Oeschger cycles on the
1009 loessic environment and malacofauna of Nussloch (Germany) during the Upper Weichselian.
1010 Quaternary Research 70, 91-104.
1011 Moine, O., Antoine, P., Hatté, C., Landais, A., Mathieu, J., Prud'Homme, C. and Rousseau, D.-D. 2017.
1012 The impact of Last Glacial climate variability in west-European loess revealed by radiocarbon
1013 dating of fossil earthworm granules. PNAS, Proceedings of the National Accademy of Sciences of
1014 the USA. Earth, Atmospheric, and Planetary Sciences, May 2017, doi: 10.1073/pnas.1614751114
1015 Mokeddem, Z. and McManus, J.F. 2016. Persistent climatic and oceanographic oscillations in the
1016 subpolar North Atlantic during the MIS 6 glaciation and MIS 5 interglacial. Paleoceanography 31,
1017 doi:10.1002/2015PA002813.
1018 Moreno, A., Svensson, A., Brooks, S.J., Connor, S., Engels, S., Fletcher, W., Genty, D., Heiri, O., Labuhn,
1019 I., Perşoiu, A., Peyron, O., Sadori, L., Valero-Garcés, B., Wulf, S., Zanchetta, G., contributors, d.,
1020 2014. A compilation of Western European terrestrial records 60–8 ka BP: towards an
1021 understanding of latitudinal climatic gradients. Quaternary Science Reviews 106, 167-185.

1022 Müller, U.C., Pross, J., Bibus, E., 2003. Vegetation response to rapid climate change in Central Europe
1023 during the past 140,000 yr based on evidence from the Füramoos pollen record. Quaternary
1024 Research 59, 235-245.
1025 Murray, A. and Wintle, A., 2000. Luminescence dating of quartz using an improved single-aliquot
1026 regenerative-dose protocol. Radiation Measurements 32 (1), 57–73.
1027 Murray, A. and Wintle, A., 2003. The single aliquot regenerative dose protocol: potential for
1028 improvements in reliability. Radiation Measurements 37 (4-5), 377-381.
1029 Obreht I., Zeeden C. Hambach U., Veres D., Marković S.B., Bösken J., Svirčev Z., Bačević N., Gavrilov
1030 M.B., Lehmkuhl F., 2016. Tracing the influence of Mediterranean climate on Southeastern
1031 Europe during the past 350,000 years. Scientific Reports, 6:36334, DOI: 10.1038/srep36334.
1032 Osipova, E., Danukalova, G., Markovic, S., 2013. Malacological characteristics of the Middle to Upper
1033 Pleistocene transitional interval (MIS 7-5) observed in the Batajnica locality (Serbia). Quaternary
1034 International 292, 86-100.
1035 Panaiotu, C.G., Panaiotu, E.C., Grama, A., Necula, C., 2001. Paleoclimatic record from a
1036 loessepaleosol profile in Southeastern Romania. Physics and Chemistry of the Earth (A) 26 (11-
1037 12), 893-898.
1038 Railsback, L.B., Gibbard, P.L., Head, M.J., Voarintsoa, N.R.G., Toucanne, S., 2015. An optimized
1039 scheme of lettered marine isotope substages for the last 1.0 million years, and the
1040 climatostratigraphic nature of isotope stages and substages. Quaternary Science Reviews 111,
1041 94-106.
1042 Radan, S.C., 2012. Towards a synopsis of dating the loess from the Romanian plain and Dobrogea:
1043 authors and methods through time. Geo-Eco-Marina 18, 153-172.
1044 Rousseau, D.-D., Antoine, P., Hatté, C., Lang, A., Zöller, L., Fontugne, M., Ben Othman, D., Luck, J.-M.,
1045 Moine, O., Labonne, M., Bentaleb, I., Jolly, D., 2002. Abrupt millennial climatic changes from
1046 Nussloch (Germany) Upper Weichselian eolian records during the Last Glaciation. Quaternary
1047 Science Reviews 21, 1577-1582.

1048 Rousseau, D.-D., Sima, A., Antoine, P., Hatté, C., Lang, A., Zöller, L., 2007. Link between European and
1049 North Atlantic abrupt climate changes over the last glaciation. Geophysical Research Letters 34,
1050 doi:10.1029/2007GL031716.
1051 Rousseau, D.-D., Antoine, P., Gerasimenko, N., Sima, A., Fuchs, M., Hatté, C., Moine, O., Zöller, L.,
1052 2011. North Atlantic abrupt climatic events of the last glacial period recorded in Ukrainian loess
1053 deposits. Climate of the Past 7, 221-234.
1054 Rousseau, D.-D., Ghil, M., Kukla, G., Sima, A., Antoine, P., Fuchs, M., Hatté, C., Lagroix, F., Debret, M.
1055 (2013). Major dust events in Europe during during Marine isotope stage 5 (130-74 ka): A climatic
1056 interpretation of the “Markers”. Climate of the Past 9, 2213-2230.
1057 Rousseau, D.-D., Boers, N., Sima, A., Svensson, A., Bigler, M., Lagroix, F., Taylor, S., Antoine, P.
1058 (2017). (MIS3 and 2) millennial oscillations in Greenland dust and Eurasian aeolian records – A
1059 paleosol perspective. Quaternary Science Reviews 169, 99 - 113.
1060 Rousseau, D.D., Svensson, A., Bigler, M., Sima, A., Steffensen, J.P. and Boers, N., (2017). Eurasian
1061 contribution to the last glacial dust cycle: how are loess sequences built? Climate of the Past 13,
1062 1181-1197.
1063 Rozycki, St. Zb., 1967. Le sens des verts portent la poussière de loess á la lumière de l’analyse des
1064 formes d’accumulation du loess en Bulgarie et en Europe Centrale. Revue de Géomorphologie
1065 Dynamique 1, 1-9.
1066 Sadori, L., Koutsodendris, A., Panagiotopoulos, K., Masi, A., Bertini, A., Combourieu-Nebout, N.,
1067 Francke, A., Kouli, K., Joannin, S., Mercuri, A.M., Peyron, O., Torri, P., Wagner, B., Zanchetta, G.,
1068 Sinopoli, G., Donders, T.H., 2016. Pollen-based paleoenvironmental and paleoclimatic change at
1069 Lake Ohrid (south-eastern Europe) during the past 500 ka. Biogeosciences 13, 1423-1437.
1070 Sánchez Goñi, M.F., Eynaud, F., Turon, J.-L., Shackleton, N.J. 1999. High resolution palynological
1071 record off the Iberian margin: direct land-sea correlation for the Last Interglacial complex, Earth
1072 and Planetary Science Letters, 171, 123-137.

1073 Sánchez Goñi, M.F., Cacho, I., Turon, J.-L., Guiot, J., Sierro, F.J., Peypouquet J.-P., Grimalt, J.,
1074 Shackleton, N.J. 2002. Synchroneity between marine and terrestrial responses to millenial scale
1075 climatic variability during the last glacial period in the mediterranean region, Climate Dynamics,
1076 19, 95-105.
1077 Sánchez Goñi, M.F., Landais, A., Fletcher, W.J., Naughton, F., Desprat, S., Duprat, J., 2008. Contrasting
1078 impacts of Dansgaard-Oeschger events over a western European latitudinal transect modulated
1079 by orbital parameters. Quaternary Science Reviews 27, 1136-1151.
1080 Schirmer, W. 2016. Late Pleistocene loess of the Lower Rhine, Quaternary International 411, 44-61,
1081 Seelos, K., Sirocko, F., Dietrich, S., 2009. A continuous high-resolution dust record for the
1082 reconstruction of wind systems in central Europe (Eifel, Western Germany) over the past 133 ka.
1083 Geophysical Research Letters 36, 1-6.
1084 Sirocko, F., Knapp, H., Dreher, F., Förster, M.W., Albert, J., Brunck, H., Veres, D., Dietrich, S., Zech, M.,
1085 Hambach, U., Röhner, M., Rudert, S., Schwibus, K., Adams, C. und Sigl, P. 2016. The ELSA-
1086 Vegetation-Stack: Reconstruction of Landscape Evolution Zones (LEZ) from laminated Eifel maar
1087 sediments of the last 60,000 years. Global and Planetary Change 142, 108-135.
1088 Stuiver, M. and Polach, H.A. (1977) Discussion: Reporting of ^{14}C data. Radiocarbon 19, 355-363.
1089 Taylor, S.N., Lagroix, F., Rousseau, D.-D. and Antoine, P., 2014. Mineral magnetic characterization of
1090 the Upper Pleniglacial Nussloch loess sequence (Germany): An insight into local environmental
1091 processes. Geophysical Journal International 199(3), 1463-1480.
1092 Timar-Gabor, A.and Wintle, A. 2013. On natural and laboratory generated dose response curves for 8
1093 quartz of different grain sizes from Romanian loess. Quaternary Geochronology 18, 34–40.
1094 Tisnérat-Laborde N, Poupeau J-J, Tannau J-F, Paterne M (2001) Development of a semi-automated
1095 system for routine preparation of carbonate samples. Radiocarbon 43, 299–304.
1096 Thompson, R. and Maher, B.A., 1995. Age models, sediment fluxes and palaeoclimatic
1097 reconstructions for the Chinese loess and palaeosol sequences. Geophysical Journal
1098 International 123, 611-622.

1099 Tzedakis, P. C., Frogley, M. R., Heaton, T. H. E., 2003. Last Interglacial conditions in southern Europe:
1100 evidence from Ioannina, northwest Greece, Global and Planetary Change 36, 157–170.
1101 Tzedakis, P. C., Hooghiemstra, H., and Pälike, H., 2006. The last 1.35 million years at Tenaghi
1102 Philippon: revised chronostratigraphy and long-term vegetation trends, Quaternary Science
1103 Reviews 25, 3416-3430.
1104 Újvári, G., Molnár, M., Novothny, A., Páll-Gergely, B., Kovács, J., Várhegyi, V., 2014. AMS ^{14}C and
1105 OSL/IRSL dating of the Dunaszekcső loess sequence (Hungary): chronology for 20 to 150 ka and
1106 implications for establishing reliable age–depth models for the last 40 ka. Quaternary Science
1107 Reviews 106, 140-154.
1108 Újvári, G., Stevens, T., Molnár, M., Demény, A., Lambert, Varga, G.,Timothy Jull, A. J., Páll-Gergely, B.,
1109 Buylaert, J.-P. and Kovácsk, J. 2018. Coupled European and Greenland last glacial dust activity
1110 driven by North Atlantic climate. PNAS. 114 (50) E10632-E10638.
1111 https://doi.org/10.1073/pnas.1712651114
1112 Varga, G., Kovács, J., and Újvári, G. 2012. Late Pleistocene variations of the background aeolian dust
1113 concentration in the Carpathian Basin: an estimate using decomposition of grain-size
1114 distribution curves of loess deposits. Netherlands Journal of Geosciences, Geologie en Mijnbouw
1115 91(1/2), 159-171.
1116 Varga, G., Cserhati, C., Kovacs, J., Szalai, Z., 2016. Saharan dust deposition in the Carpathian Basin
1117 and its possible effects on interglacial soil formation. Aeolian Research 22, 1-12.
1118 Vandenberghe, J., Huijzer, A.S., Mücher, H., Laan, W., 1998. Short climatic oscillations in a western
1119 European loess sequence (Kesselt, Belgium). Journal of Quaternary Sciences 13, 471-485.
1120 Vandenberghe, J. 2013. Grain size of fine-grained windblown sediment: A powerful proxy for process
1121 identification. Earth Science Reviews 121, 18-30.
1122 Yang, S., and Ding, Z. (2014). A 249 kyr stack of eight loess grain size records from northern China
1123 documenting millennial-scale climate variability. Geochenmistry, Geophysics, Geosystems
1124 15(3), 789-814.

Zhou, L.-P., Oldfield, F., Wintle, A.G., Robinson, S.G. and Wang, J.T., 1990. Partly pedogenic origin of magnetic variations in Chinese loess. Nature 346, 737-739.

Figures titles and captions

Fig. 1. Loess distribution in Europe. A) Location of the Lower (LDL) and Middle Danube (MDL) loess area and of Northern France and Belgium (NF-BL) loess area, in a simplified map of the European loess belt. B) Location of the Harletz and of other main regional loess-palaeosol sequences from Serbia to the Black Sea (loess map: according to Antoine et al., 2013, modified from Haase et al., 2007).

1) Aeolian sands, 2) Sandy loess, 3) Loess (> 5 m), 4) Loess (< 5 m), 5) Some palaeo-wind directions from the Lower Danube loess area according to Rozycki, 1967.

Fig. 2. Detailed location and geomorphology of the Kozloduy-Harletz area. Location of the Harletz-2012 (HZ12) section and of the cross-section of Fig. 3 (topography according to *Google Earth Pro 2018*, *Image © 2015 CNES / SPOT image*).

Fig. 3. Stratigraphical cross-section of the right bank of the Danube River valley highlighting fluvial terraces (T1 and T2) and loess cover. Location of the Harletz profile on the T2 terrace according to topographic and stratigraphic data (redrawn from Evlogiev, 2015).

1) Fluvial sands and gravels, 2) Fluvial silts and clays (T0), 3) Fluvial sandy silts (T1) and clayey sandy silts (T2), 4) Loess and sandy loess, 5) Palaeosol horizons, 5) Top soil (chernozem).

Fig. 4. General view of the Harletz section during preparation works, showing the succession of the vertical steps making the profile (photograph taken by M. Fuchs).

Fig. 5. Detailed stratigraphic log of the Harletz profile including the location of the various luminescence and micromorphological samples (blocks). High-resolution grain size data (clay, coarse and fine sand, grain size ratios (GSI and CSI), TOC, carbonate, mass-specific magnetic susceptibility (χ_{BULK} in 10^{-8} m^3/kg) and absolute frequency dependence of mass-specific magnetic susceptibility ($\Delta\chi_{FD}$ in 10^{-8} m^3/kg), colour reflectance data and luminescence dating results from Lomax et al. (2018) (black: feldspar coarse grain fraction, applying the MET-pIRIR protocol, grey italics: quartz fine grain fraction and SAR protocol).

Detailed description of the units: see table 1.

Fig. 6. Micromorphology description of Harletz thin sections (location of samples: see Fig. 5)

A to D: Ogosta Soil Complex.

A and D: sample B3 – rock fragment, PPL and XPL;

B: sample B3 – The sediment consists mainly of quartz silt and sand. Muscovite and other minerals are abundant. No visible bedding. The sediment is strongly bioturbated with a channel microstructure, and rounded aggregates. Biological cavities can exceed a few centimeters in diameter.

C: sample B2 – on the left, vertical biological channel intersecting the bedding on the right. The sediment consists essentially of quartz sand and silt, with numerous muscovite and other minerals.The bedding is of sedimentary origin. The walls of the channel are lined with fine particles.

E to I: Lower loess (unit 3b and 4)

E and F - sample B8, calcareous loessic deposit. Channels are numerous but very small, less than a few millimetres long. E: quartz silt, micas (muscovite and biotite) and carbonates. F: detail of carbonates grains.

G to I – sample B4, calcareous loessic deposit. G: The sediment is much less bioturbated than in B8. Weak channel microstructure. No aggregates, PPL; H : quartz and calcite grains; numerous micas, XPL; I : bioturbation with silty deposit, PPL;

J to L: Harletz Soil Complex.

J and K, sample B5. J: quartz silt and sand; mainly porphyric related distribution; subangular blocky microstructure, mixed with channel and chamber microstructure; in chambers, granular microstructure (pellets). No coatings; K: in the middle, feldspar.

L, sample B6: mainly enaulic related distribution, locally a tendency to chitonic or porphyric related distribution. Granular microstructure probably resulting from biological activity, mixed locally with blocky microstructure. Numerous little channels, for most of them empty.

Fig. 7. A bivariate plot of the absolute frequency dependence of mass specific magnetic susceptibility ($\Delta\chi_{FD}$) and the bulk mass specific magnetic susceptibility (χ_{BULK}) of all 400 5 cm sampling depth intervals. The variables are linearly correlated with an R^2 of 0.96, a slope of 0.12 and a y-intercept of -3.02 x 10^{-8} m^3/kg. See Section 3.3 for discussion of results.

Fig. 8. Bivariate plots comparing and cross-checking three proxies (clay %, a*, and $\Delta\chi_{FD}$) of degree of pedogenesis: (A) clay % against a*, (B) clay % against $\Delta\chi_{FD}$, and (C) $\Delta\chi_{FD}$ against a*. See Section 3.3 for discussion of results.

Fig. 9. Cumulative grain size curves of A: typical loess samples from Unit 3b (between 11 and 10m) and B: samples from the lower soil horizon (2b) of the Harletz Soil Complex (between 6 and 5m). Legend names are depths in centimetres.

Fig. 10. Stratigraphic correlations between the Harletz sequence and some main references sequences from Serbia (Markovic et al., 2015), Bulgaria (Koriten, Jordanova and Petersen, 1999), Romania (Balescu et al., 2010). Comparison with a synthetic loess-palaeosol record for North Western Europe (France to Belgium, according to Antoine et al., 2016, Meijs, 2002).

(1 to 5: Western European sequence only).

1 (BLS and BLS Cpx.) Brown leached soils and soil complexes: Bt horizon (s) of brown leached soil (s). 2 (HSC 1 and 2) Humic soil complexes: grey forest soils and steppe soils complexes. 3 (BSC): Boreal to arctic brown soil complex. 4 (G) Tundra gley horizons. 5) Large ice-wedge casts with loess infilling. 6) Interglacial Chernozem soil horizons. 7) Weakly developed interstadial "steppe soils" (*IS / L1SS1*): Interstadial soils and soil complexes. 8) Penultimate glacial (Saalian / MIS 6) loess. 9) Accumulation of secondary $CaCO_3$ (CCa). 10 (Harletz) Bt to Bw horizon of luvic Cambisols developed on alluvial sandy silts. 11 (Harletz) Intensely bioturbated Bv horizon of interglacial Cambisol. 12 (Harletz) strongly bioturbated luvic Cambisol to luvic Phaeozem.

Fig. 11. Variation of absolute frequency dependence of mass specific magnetic susceptibility ($\Delta\chi_{FD}$ in 10^{-8} m^3/kg), a* (colour reflectance), clay percentages and Grain size index (GSI) throughout the Harletz loess-palaeosol record. Attempt of correlation with MIS stages and LR-04 Global $\delta^{18}O$ stack (Lisiecki and Raymo, 2005).

According to strong variations in sedimentation rates in the record, the LR-04 chronology has been segmented in three parts: (1) From ca.10 to 75 ka (Weichselian Pleniglacial and Late glacial) in light grey), (2) from 75 to 130 (Eemian interglacial and Weichselian Early-glacial in dark grey) and (3) from 130 to 230 (Late Saalian and younger part of the Penultimate interglacial (MIS 7), in black).

Fig. 12. Attempt of correlation between the Saalian part of the Harletz section, CSI and a* with the Lake Ohrid record and chronology (TOC and percentage of mesophylous species, according to Francke et al., 2016 and Sadori et al., 2016). Comparison with MIS stages (LR-04) and sub-stages (Railsback et al., 2015), and the high-resolution record of $\delta^{18}O$ of *G. bulloides* from Eastern Atlantic (Iberian Margin), according to Hodel et al., 2013.

Fig. 13. A) Geomorphology of the Kozloduy-Harletz loess area, with location of the likely silt and sand sources area (alluvial plains) and palaeo-wind directions, location of the transect of **Fig. 13B**

(topography according *Google Earth Pro 2018, Image © 2015 CNES / Astrium*). 1) Main loess gredas 2) dry valleys separating the gredas, 3) Main W-NW palaeo-wind direction, 4) Secondary E-NE palaeo-wind directions. **B)** NW-SE topographic cross section from the Danube alluvial plain to the Ogosta River at Harletz. Showing deflation area, transport distance and deposition zone (red dotted arrows).

Tables titles and captions

Table 1

Stratigraphy of the Harletz loess sequence: description of the Units and pedosedimentary interpretation, from top to bottom

Sample depth (cm / top)	Clay (<2µm) (%)	Fine silt (%) (2-20µm)	Coarse silt (%) (20-50µm)	Fine sand (%) (50-200 µm)	Coarse sand (%) (200-2000 µm)
22.50	21.5	26.3	37.8	13.3	1.1
102.50	18.9	23.6	41.2	15.3	1.0
252.50	21.3	26.7	35.3	13.9	2.8
352.50	20.1	25.1	38.2	16.1	0.5
452.50	29.2	23.7	28.0	12.7	6.4
552.50	31.5	24.2	28.1	12.4	3.8
652.50	19.2	23.3	39.0	17.3	1.2
902.50	13.1	19.8	45.0	21.9	0.2
1112.5	11.7	18.5	48.2	21.4	0.2
1312.5	19.7	22.2	38.4	18.4	1.3
1357.5	15.2	23.3	43.3	17.7	0.5
1482.5	22.1	25.0	34.6	15.3	3.0
1552.5	24.9	24.0	32.0	17.4	1.7
1622.5	27.9	20.5	25.0	17.0	9.6

1722.5	27.6	18.5	29.4	21.4	3.1
1802.5	27.1	18.9	29.7	22.0	2.3
1902.5	28.9	18.1	29.3	14.2	9.5

Table 2

Percentages of the five main grain size classes (from clay to coarse sand) for a set of 17 reference samples analysed using the classical sieving and pipetting method

Sample	Depth (m)	Unit	Water (%)	n (Q / FS)	D_e (Gy) Q	FS	U (ppm)	Th (ppm)	K (%)	Dose rate (Gy/ka) Q	FS	Age(ka) *Q*	**FS**
Gi05	1.35	1b	12	6/5	142± 5	141 ± 7	3.85± 0.32	9.52± 1.05	1.52± 0.08	3.56± 0.21	3.65± 0.23	*40±3*	**39±3**
Gi06	2.80	1c	-	-/-	-	-	3.76± 0.32	8.59± 1.00	1.47± 0.07	-	-	-	-
Gi07	4.00	1d	12	6/8	197± 6	217 ± 9	4.12± 0.29	7.59± 0.96	1.53± 0.08	3.43± 0.21	3.53± 0.23	*57±4*	**62±5**
Gi08	4.45	2a	15	6/-	227± 7	-	3.34± 0.30	7.48± 0.93	1.50± 0.08	3.06± 0.18	-	*74±5*	-
Gi09	5.20	2b	15	6/6	267± 9	252 ± 14	3.26± 0.26	7.53± 0.85	1.39± 0.07	2.93± 0.17	3.07± 0.20	*91±6*	**82±7**
Gi10	7.60	3b	12	6/5	297± 10	485 ± 30	3.46± 0.28	9.07± 0.94	1.50± 0.07	3.29± 0.20	3.40± 0.22	*90±6*	**142±13**
Gi11	8.70	3b	12	6/4	320± 10	480 ± 22	3.58± 0.28	8.48± 0.91	1.50± 0.08	3.27± 0.20	3.38± 0.22	*98±7*	**142±11**
Gi12	9.90	3b	12	4/5	339± 13	502 ± 17	3.04± 0.31	10.90± 1.01	1.49± 0.07	3.30± 0.20	3.41± 0.23	*103±7*	**147± 11**
Gi13	11.45	3b	12	-/5	-	579 ± 28	3.69± 0.30	8.52± 0.98	1.50± 0.07	-	3.39± 0.23	-	**171±14**
Gi14	12.80	5	12	6/-	324± 13	-	3.94± 0.30	8.53± 1.00	1.60± 0.08	3.45± 0.21	-	*94±7*	-
Gi15	14.05	8	12	6/-	339 ± 14	-	4.01± 0.31	8.95± 1.03	1.64± 0.08	3.54± 0.22	-	*96±7*	-
Gi16	14.10	9	15	-/-	-	-	4.32± 0.30	7.64± 0.97	1.64± 0.08	-	-	-	-
Gi17	15.55	11	15	6/5	331± 11	429 ± 16	3.30± 0.33	10.62± 1.08	1.42± 0.07	3.16± 0.19	3.28± 0.22	*105±7*	**131±10**
Gi18	17.55	13a	20	6/-	345± 13	-	4.34± 0.29	7.15± 0.94	1.40± 0.07	2.99 ± 0.18		*115±8*	-
Gi19	18.40	13b	20	6/-	355± 12	-	3.80± 0.27	8.29± 0.90	1.47± 0.07	2.99 ± 0.18		*119±8*	-
Gi20	19.75	14	25	5/5	332± 12	469 ± 19	3.66± 0.26	7.61± 0.86	1.77± 0.09	2.99± 0.17	3.14± 0.20	*111±7*	**149±11**

Table 3

Luminescence age determinations from Lomax et al. (2018) (Q**:** quartz, **FS**: Feldspar)

Sample	Mollusc species (>>> markedly dominant species)	Interpretation
HZ-12 -5.9-6.0m Unit 2b	1) >>> Cernuella cf. virgata (Da Costa, 1778) *2) Chondrula tridens* (Müller, 1774) *3) Helicopsis striata* (Müller, 1774) or *Candidula rhabdotoïdes* (Wagner, 1928) 4) *Punctum pygmaeum* (Draparnaud, 1801)	Dry soil with grassland developed under a temperate (interglacial ?) climate (*Punctum pygmaeum*).
HZ 12 -16.05 to -16.25 m Unit 12.	*1) >>> Chondrula tridens* (Müller, 1774) *2) Granaria frumentum* (Draparnaud, 1801) *3) Cernuella sp.* *4) Cepaea sp.* *5) Helicopsis striata* (Müller, 1774) *6) Candidula rhabdotoïdes* (Wagner, 1928).	Dry and well-drained environment. Relatively well-developed vegetal cover developed under interglacial conditions with some arboreal vegetation very likely (*Cepaea* sp.)

Table 4

Malacological assemblages from two test samples collected in Units 2b and 12; interpretation of local environmental and climatic conditions (determination by Jitka FRODLOVA, University of Brno, Czech Republic). For each sample the species (n°1 to n°6) are presented by decreasing relative abundance

Sample ref.	Depth (m)	Lab. Ref.	Age yr. BP (1sigma)
Hz 3.0 – 3.1	3.0 – 3.1	GifA-14362/SacA-40166	35270 ± 190
Hz 5.6 – 5.7	5.6 – 5.7	GifA-14363/SacA-40167	36840 ± 220
Hz 6.8 – 6.9	6.8 – 6.9	GifA-14364/SacA-40168	37490 ± 190

Table 5

Radiocarbon analysis of mollusc shells (*Helicopsis striata*)

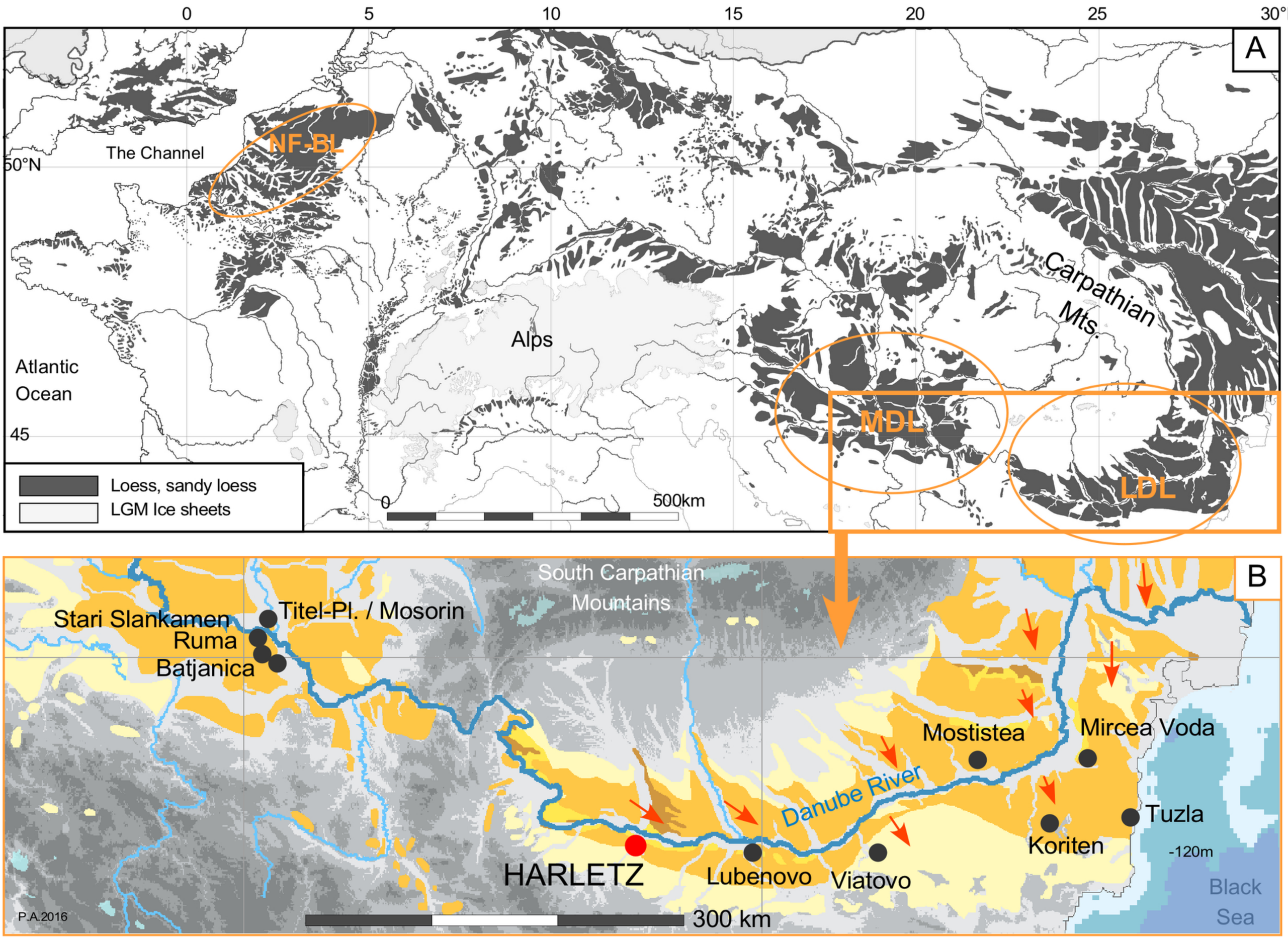
0
5
10
15
20
25
30°
A
NF-BL
The Channel
50°N
Alps
Carpathian
Mts.
Atlantic
Ocean
45
MDL
LDL
Loess, sandy loess
LGM Ice sheets
0
500km
B
South Carpathian
Mountains
Stari Slankamen
Ruma
Batjanica
Titel-Pl. / Mosorin
Mostistea
Mircea Voda
Danube River
Tuzla
Koriten
-120m
HARLETZ
Lubenovo
Viatovo
Black
Sea
P.A.2016
300 km
0 to 200m
200 to 500m
> 500m
1
2
3
4
5

N

Cross section
Fig. 3

Alluvial plain (T0)

Alluvial plain

Danube River

24m

T1

T0

T2

Slope

Kozloduy
Nuclear
Power Plant

50 m

35m

50m

24m

Ogosta Riv.

Meanders
eroding loess
cover

70m

95m

Loess Plateau

75m

Harletz

60 m

Loess Plateau
with elongated
loess ridges
(Greda morphology)

3km

Harletz
profile 2012

Alluvial
plain

30m

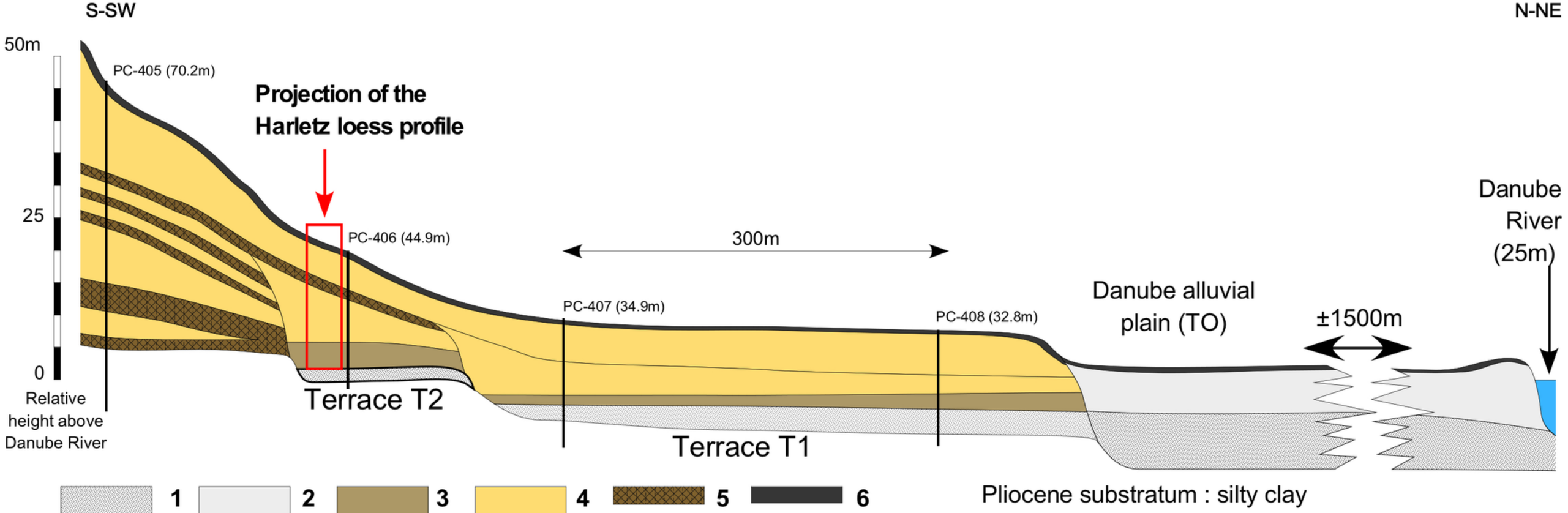
S-SW
N-NE
50m
25
0
Relative height above Danube River
PC-405 (70.2m)
Projection of the Harletz loess profile
PC-406 (44.9m)
300m
PC-407 (34.9m)
PC-408 (32.8m)
Danube alluvial plain (TO)
±1500m
Danube River (25m)
Terrace T2
Terrace T1
1
2
3
4
5
6
Pliocene substratum : silty clay

HARLETZ 2012

X-bulk (10^{-7} m^3/kg) 20 40 60 80 100

TOC (%) 0 0.1 0.2 0.3 0.4

0.4 to 1.6 % in units 1a-0

Coarse sand (> 160 µm %) 0 5 10 15 20

Coarse silt / fine silt ratio (CSI) 0.4 0.6 0.8 1.0 1.2 1.4 1.6 1.8

Subsequence 2

Subsequence 1

0 1a 1b 1c 1d 2a 2b 3a 3b 4 5 6 7 8 9 10 11 12 13a 13b 14

0 2 4 6 8 10 12 14 16 18 20m

40±3
39±3
57±4
62±5
74 ± 5
91 ± 6
82 ± 7
142 ± 13
142 ± 11
147 ± 11
171 ± 14
*131 ± 10 **
*149 ± 11 **

Harletz Soil Cpx.

HZ-SL-3

HZ-SL-2

HZ-SL-1

Tephra (162 ± 6)*

Ogosta Soil Complex

B1 B2 B3 B4 B5 B6 B7 B8 B9 B10

P.A.2012

Spectrocolorimetry a*(d65) 4 5 6 7 8 9

Δ X_{fd} 10^{-8} m^3/kg 2 4 6 8 10

Clay (< 6 µm %) 10 15 20 25 30 35 40

$CaCO_3$ % 5 10 15 20 25

Fine sand (63-160 µm) 5 10 15 20 25

GSI (CS+FS/clay) 0 0.5 1.0 1.5 2.0

Luminescence sample Undisturbed blocks

(162±6)*: Vico-b Tephra according to Baumgarten et al., 2016 Radiocarbon / mollusc shells Test sample (% 200-2000µm)

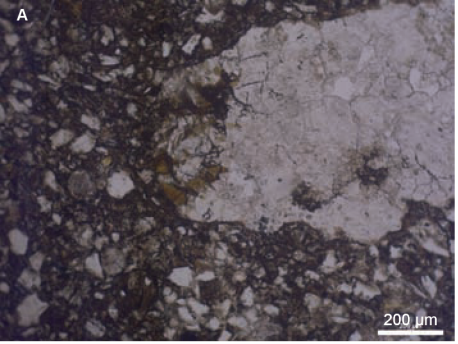
A
200 µm

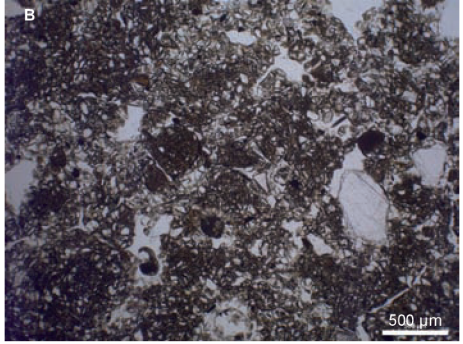
B
500 µm

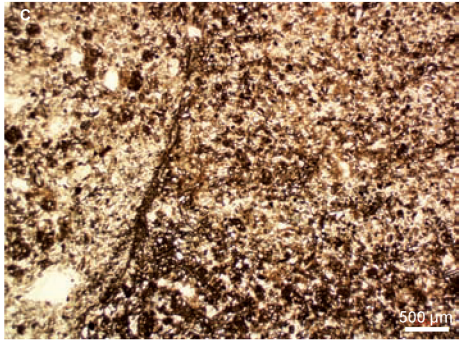
C
500 µm

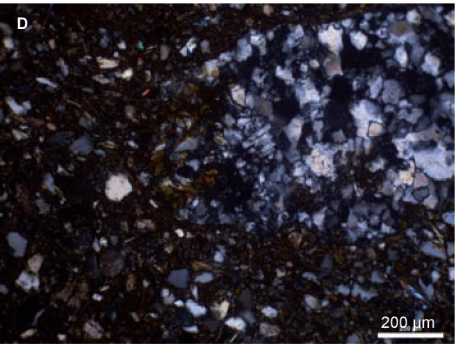
D
200 µm

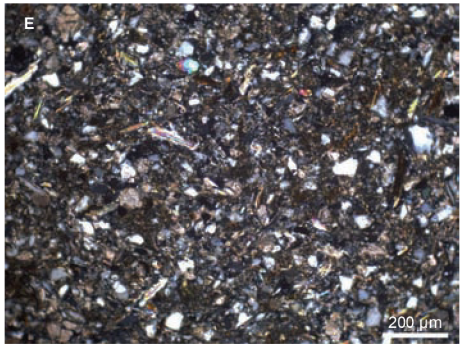
E
200 µm

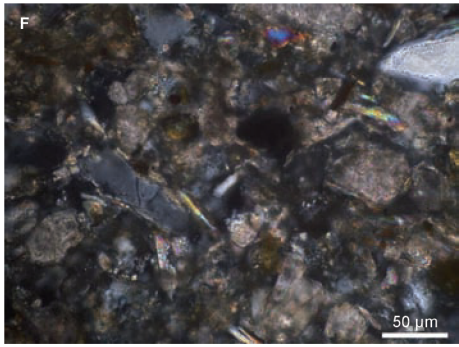
F
50 µm

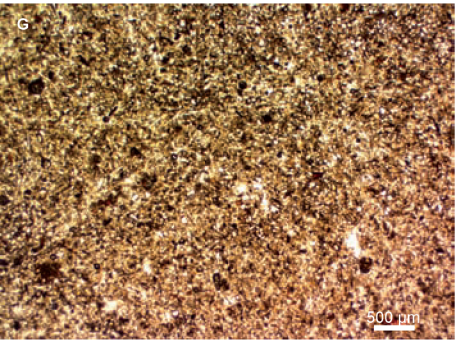
G
500 µm

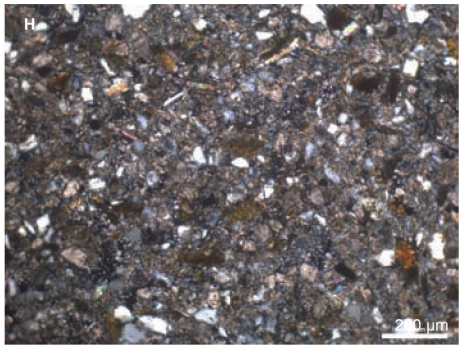
H
200 µm

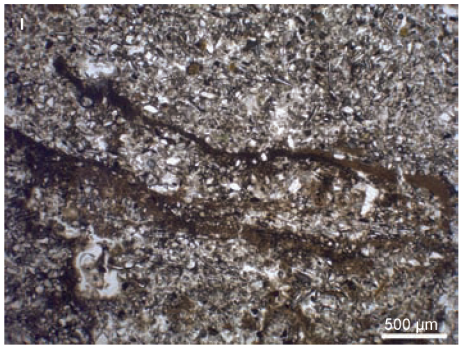
I
500 µm

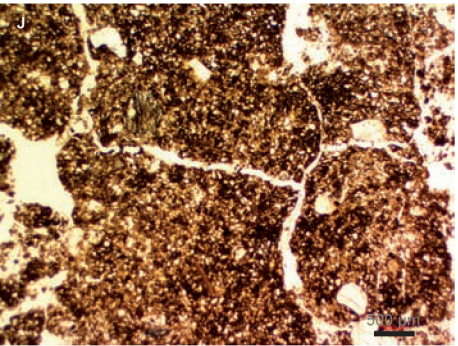
J
500 µm

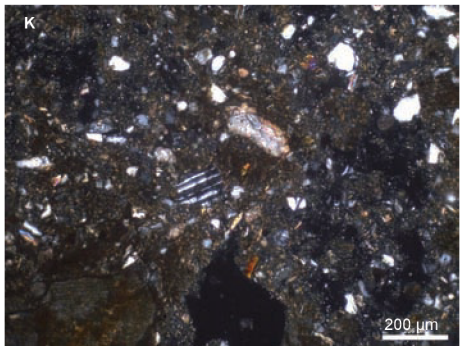
K
200 µm

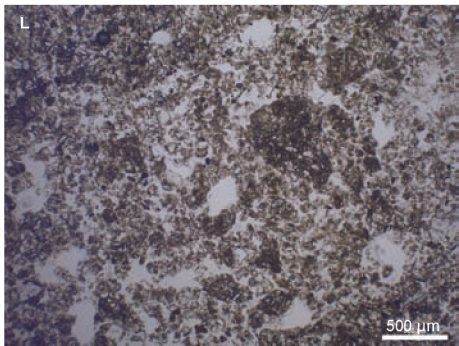
L
500 µm

Units 0, 2, 12, 13

Units 1a-c, 10, 11, 14

Units 1d, 3-9

$\Delta\chi_{FD}$ (m^3/kg)

χ_{BULK} (m^3/kg)

0

2 10^{-8}

4 10^{-8}

6 10^{-8}

8 10^{-8}

1 10^{-7}

0

2 10^{-7}

4 10^{-7}

6 10^{-7}

8 10^{-7}

1 10^{-6}

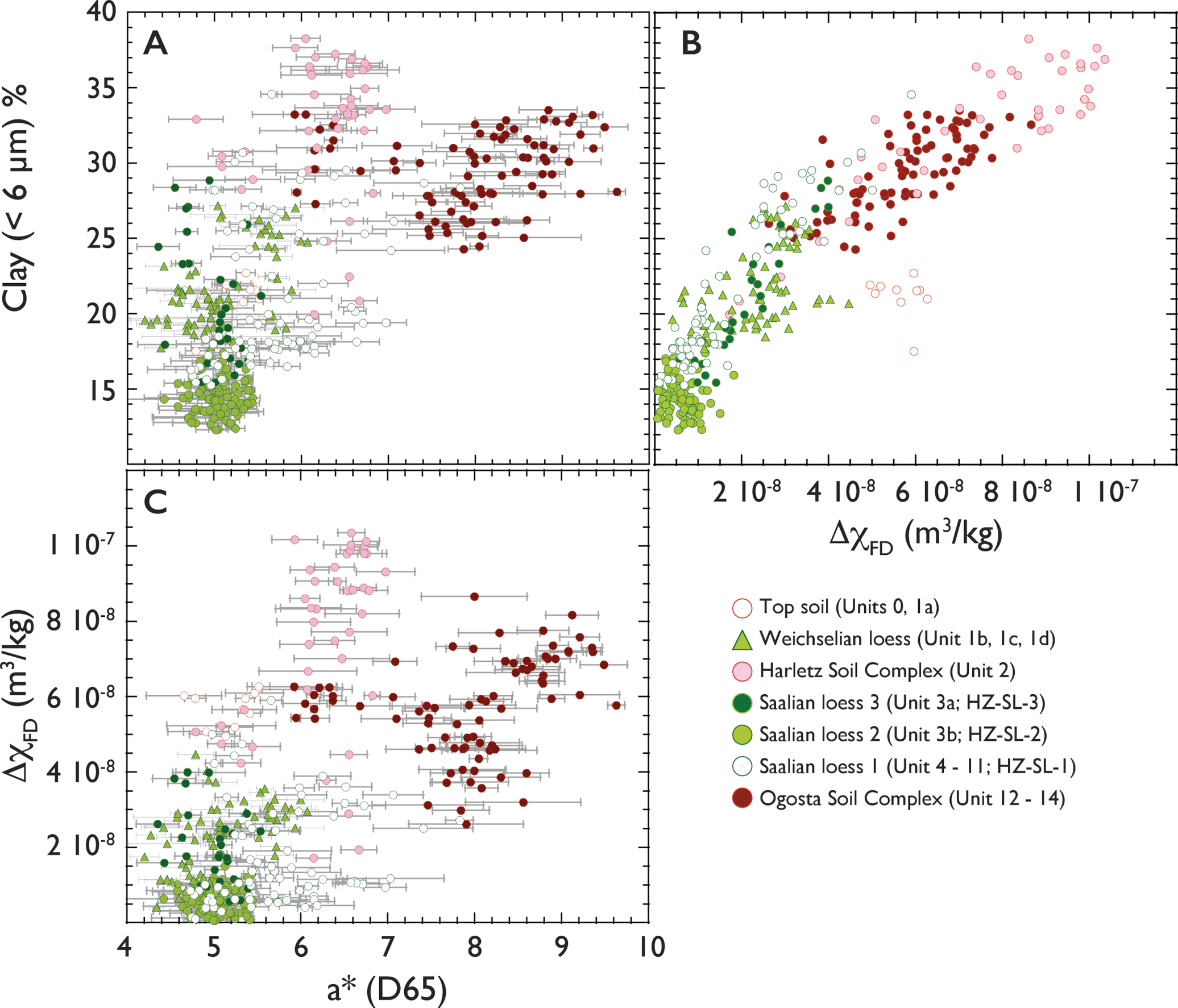
A
B
C
Clay (< 6 µm) %
40
35
30
25
20
15
2 10-8
4 10-8
6 10-8
8 10-8
1 10-7
Δχ_FD (m³/kg)
4
5
6
7
8
9
10
a* (D65)
Top soil (Units 0, 1a)
Weichselian loess (Unit 1b, 1c, 1d)
Harletz Soil Complex (Unit 2)
Saalian loess 3 (Unit 3a; HZ-SL-3)
Saalian loess 2 (Unit 3b; HZ-SL-2)
Saalian loess 1 (Unit 4 - 11; HZ-SL-1)
Ogosta Soil Complex (Unit 12 - 14)

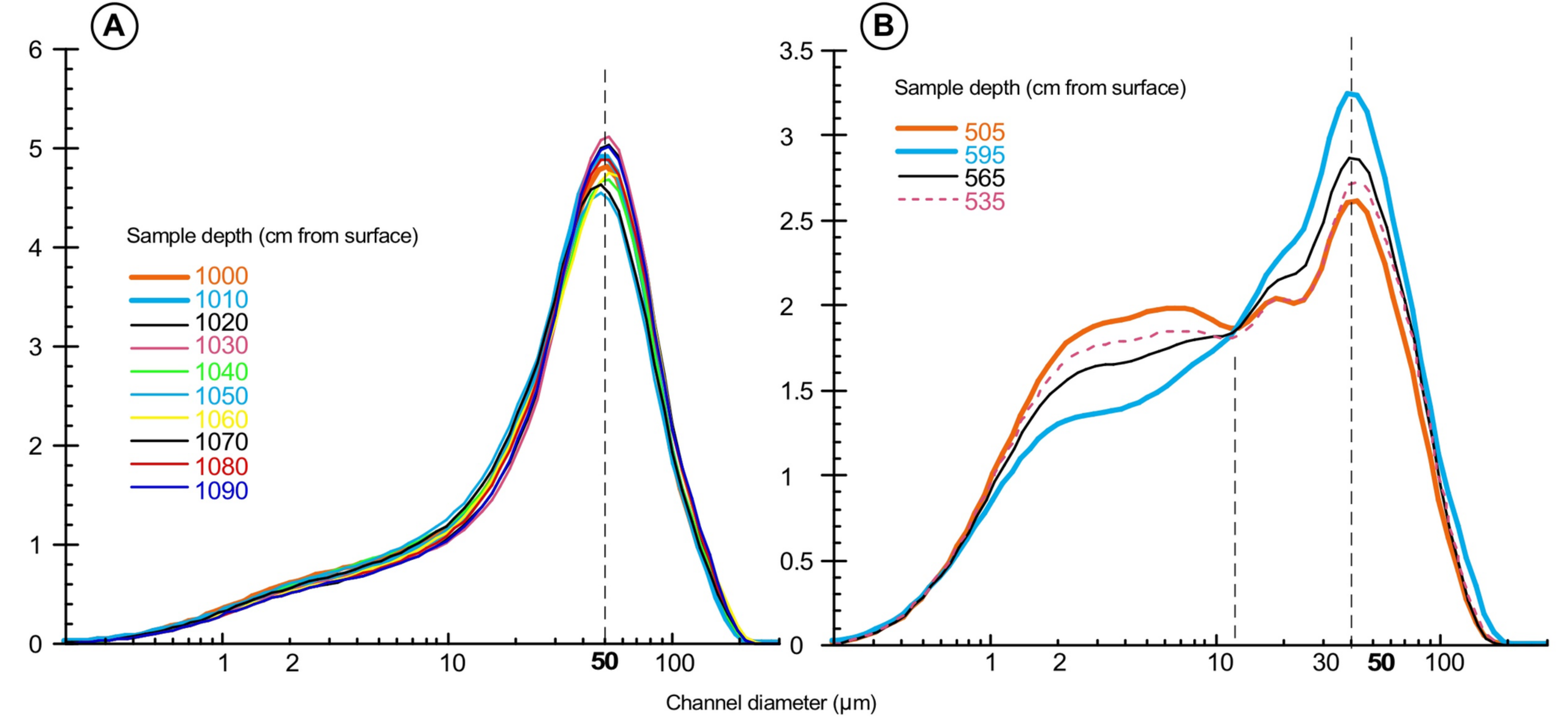
A
Sample depth (cm from surface)
1000
1010
1020
1030
1040
1050
1060
1070
1080
1090
0
1
2
3
4
5
6
1
2
10
50
100
B
Sample depth (cm from surface)
505
595
565
535
0
0.5
1
1.5
2
2.5
3
3.5
1
2
10
30
50
100
Channel diameter (µm)

MIS

Belgium & N.-France*

Titel Plateau (Serbia)

Harletz (Hz.12) (Bulgaria)

Koriten Core (Bg.)

Mircea-Voda (Romania)

Mostistea (Romania)

0
2
4
6
8
10
12
14
16
18
20
22
24m

1
2
3
4
5
6
7
8

G
G
G
BSC (cpx.)
HSC 1
BLS
G5
G4
G3
G2
G1
HSC 2
BLS
Cpx.

L1LL1
IS / L1SS1 (cpx.)
L1LL2
Fs1 (Cpx.)
L2
T.layer
ESL
Fs2 (cpx.)
L3

40±3
39±3
IS (cpx.)
57±4
62±5
74±5
91±6
82±7
Harletz Soil Complex
142±13
142±11
147±11
171±14
T. layer (162±6)
Hz-TS4
Hz-IS3
Hz-IS2
Hz-IS1
131±10*
Ogosta Soil Complex
149±11*
Alluvial dep.

L1
Fs1
L2
-14.8
Fs2 (cpx.)
L3

• 26±3
SL-1
L1
S1
L-2
• 179±16
IS
S2 (cpx)
L3
• 279±41

L1
• 67±5
S1
• 132±14
L-2
• 171±22
IS
S2cpx
L3
• 281±43

T.layer

1 2 3 G 4 5
6 IS -ESL 7 8 9
10 11 12

HARLETZ 2012

ΔX_{fd} 10^{-8} m^3/kg

GSI (CS+FS/clay)

MIS

$D^{18}O$ Stack LR-04 (‰)

Age(ka)*

40±3
39±3
57±4
62±5
74±5
91±6
82±7
142±13
142±11
147±11
171±14
Tephra (162±6)*
131±10*
149±11*

Interglacial-Early-glacial Soil Cpx

Interglacial Soil Cpx

Spectrocolorimetry a*(d65)

Clay (< 6 µm %)

P.A 2012

luminescence ages (feldspar)

Harletz CSI (coarse silt / fine silt ratio)

ka L.Oh.

Lake Ohrid mesophylous (%)

MIS*

MD 01-2444 $\delta^{18}O$ (*G. Bulloides*)

Hz-SL3

Hz-SL2

Hz-SL1

142±13

142±11

147±11

171±14

162±6 (Vico-b T.)

*131±10**

OD4

OD5

OD6

6a

6b

6c

6d

6e

7a

Harletz Colour reflectance a*(d65)

Lake Ohrid TOC

Ka (MD 01-2444)

A

N

Cross section:
inset B

24m

Alluvial plain (T0)

Danube River

Kozloduy
Nuclear
Power Plant

T1

T2

T3

50 m

35m

50m

70m

95m

75m

Loess Plateau

24m

Alluvial
plain

Ogosta Riv.

Greda

Greda

Harletz
60 m

Harletz
Profile 2012

Harletz (bulgaria)
30m

1 2

3 4

1 km

B

NW

70m Danube : 2 km

Deflation

T0 T1 T2 T3

Harletz Profile

SE

Deposition

Ogosta

30

0 1500 m